Effect of porosity variation strategy on the performance of functionally graded Ti-6Al-4V scaffolds for bone tissue engineering

Zhang, Xiang Yu; Fang, Gang; Xing, Lei Lei; Liu, Wei; Zhou, Jie

DOI
10.1016/j.matdes.2018.07.064

Publication date
2018

Document Version
Accepted author manuscript

Published in
Materials and Design

Citation (APA)
Zhang, X. Y., Fang, G., Xing, L. L., Liu, W., & Zhou, J. (2018). Effect of porosity variation strategy on the performance of functionally graded Ti-6Al-4V scaffolds for bone tissue engineering. *Materials and Design*, *157*, 523-538. https://doi.org/10.1016/j.matdes.2018.07.064

Effect of porosity variation strategy on the performance of functionally graded Ti-6Al-4V scaffolds for bone tissue engineering

Xiang-Yu Zhang[1], Gang Fang[1,] *, Lei-Lei Xing[2], Wei Liu [2], Jie Zhou [3]

[1] State Key Laboratory of Tribology, Department of Mechanical Engineering, Tsinghua University, Beijing 100084, China

[2] School of Materials Science and Engineering, Tsinghua University, Beijing 100084, China

[3] Department of Biomechanical Engineering, Delft University of Technology, Mekelweg 2, 2628 CD Delft, The Netherlands

*Corresponding author, Gang Fang: Tel: +86-10-6278 2694, E-mail: fangg@tsinghua.edu.cn

Abstract

Functionally graded scaffold (FGS) is designed to mimic the morphology, mechanical and biological properties of natural bone closely. Porosity variation strategy between different regions in FGS plays a crucial role in influencing its mechanical and biological performance. A combination of modeling tool and scripting language can effectively enhance the ability to optimize FGS designs. This study was aimed at determining the effect of porosity variation strategy on the mechanical performance and permeability of the as-built and as-heat-treated FGSs. Ti-6Al-4V FGSs with sizes of 10×10×15 mm and diamond lattice structures were designed and fabricated by means of selective laser melting. A wide range of porosities in the FGSs (38~75%) were achieved by applying six different porosity variation strategies. The elastic modulus (3.7~5.7 GPa) and yield strength (27.1~84.7 MPa) of the as-built FGSs were found to vary between the corresponding mechanical properties of cancellous bone and cortical bone. Heat treatment reduced the strengths by 13~56%. Porosity variation strategy strongly affected the deformation behavior and failure mechanisms of the FGSs. The sigmoid function-controlled FGSs showed gradual failure behavior and

sample Sigk0.5b8 showed superior overall performance. The results demonstrated that porosity variation strategy is a feasible means for tailor design of FGS.

Keywords: functionally graded scaffold; selective laser melting; Ti-6Al-4V; mechanical properties; permeability

1. Introduction

Human bone performs diverse mechanical, biological and chemical functions, such as structural support, protection and storage of healing cells and mineral ion homeostasis. It has complex hierarchical structures at different scales [1]: whole bone level, architectural level, tissue level, lamellar level and ultrastructure level. Human skeleton is made of two types of osseous tissues, i.e., cortical bone and cancellous bone, which differ in their structure and distribution. Cancellous bone has a spongy structure that is mostly distributed in the inner part of bone. It is highly porous (porosities between 50% and 90%) and consists of a large number of trabeculae. Cortical bone, which constitutes up to 80% of the weight of human skeleton, on the other hand, has a porosity of less than 10% and is much stronger than cancellous bone. The structural differences between cortical bone and cancellous bone lead to apparent disparities in their mechanical properties. The stiffness and yield strength values of human cancellous bone and cortical bone range from 0.1-4.5 to 3-20 GPa and from 2-17 to 33-193 MPa, respectively [2, 3].

Bone tissue engineering (BTE) scaffold is a porous structure that acts as a template for bone tissue formation during the healing of segmental bone defect. It may be cultured in vitro to synthesize tissues and then implanted into the injured site. Alternatively, it may be implanted directly into the injured site, using the body's own systems, where the regeneration of tissues is induced in vivo. BTE scaffold with an appropriate elastic modulus, when subjected to biophysical stimuli, eliminates the stress shielding effect and promotes the growth of bone tissue simultaneously. Ideal BTE scaffold is able to meet the following performance requirements [4]: good biocompatibility; appropriate pore sizes and porosity that are suitable for bone cell infiltration and growth;

comparable mechanical properties with adjacent bone tissue; osteoconductivity and osteoinductivity and biodegradability. To fulfill parts of the above requirements, BTE scaffold must have a porous structure for the ingrowth of bone tissue and the reduction of the stress shielding effect. Such a complex structure can hardly be realized by using conventional fabrication technologies.

Additive manufacturing (AM), as an alternative fabrication technology, has, in recent years, gained much attention. It offers the advantages of high processing flexibility and high material utilization rate and thus it is especially suitable for the fabrication of patient-specific implants [5]. Because AM is capable of generating highly-porous structures on the scale of micrometers, it has been extensively adopted in the research on BTE scaffolds [6-9].

BTE scaffold designed to replace a segment of load-bearing bone should have sufficient strength and long fatigue life. Synthetic polymers, such as polylactic acid (PLA) and polyglycolic acid (PGA), have insufficient mechanical strength and stiffness [10], which disqualifies them as the suitable materials for load-bearing BTE scaffolds. By means of selective laser melting (SLM) or electron beam melting (EBM), metallic materials can be processed into highly porous scaffolds with sufficient stiffness and strength [11]. The dominant method currently used for scaffold design is to generate a three-dimensional (3D) periodic porous structure by replicating one or more kinds of polyhedrons [12, 13]. The study of Gibson and Ashby [14] revealed that the mechanical properties of a porous biomaterial are closely related to its density. Since this pioneering research, numerous experimental studies have been conducted to investigate the correlations between the porosity and mechanical behavior of BTE scaffolds [15-17]. Most of researchers have adopted the bottom-up approach; to construct a 3D scaffold, unit cells are made and then assembled. In general, unit cells can be classified into two categories, based on their main deformation mechanism, namely bending-dominated unit cells and stretching-dominated unit cells. The stiffness and strength of a stretch-dominated structure depend linearly on its porosity and are generally higher than those of a

bending-dominated porous structure [18].

The focus of most of the preceding studies has been placed on the characterization of the mechanical properties of scaffolds with uniform porous structures. However, to treat a large-scale segmental bone defect, a BTE scaffold that mimics the structures of both cancellous bone and cortical bone is desired. In other words, a scaffold with a uniform porous structure may not meet the complex and diverse requirements in mechanical and biological performance the best. Functionally graded scaffold (FGS) with varying structures similar to those of native bone tissues may provide biological and mechanical functions better. It is thus of great interest to develop strategies for FGS design and evaluate the mechanical and biological performances of various FGSs.

The types of designed FGSs that have so far been developed are as follows:

1) FGS is designed to have struts with varied diameters. A non-stochastic scaffold is mostly composed of a large number of unit cells, which further consist of dozens of struts. Varying strut diameter is an effective and feasible way to achieve desired variations in pore size and porosity. Grunsven et al. [19], for example, manufactured three-layer graded lattice structures, where the strut thickness in each layer increased in the axial direction. Mechanical tests of such scaffolds revealed that the mechanical behavior of the graded structures could be predicted by the rule of mixtures. Han et al. [20] fabricated similar three-layer graded porous titanium scaffolds based on the Schwartz diamond unit cell with strut diameters of 483-905 μm and their elastic moduli and yield strengths were tailored over ranges of 0.28-0.59 GPa and 3.79-17.75 MPa, respectively. To achieve more uniformly linear gradient scaffolds, Maskery et al. [21] produced graded density lattice structures by gradually increasing strut diameter and investigated the effect of heat treatment on the mechanical behavior. Nune et al., [22] studied the functional response of osteoblasts in functionally axial gradient titanium scaffolds. Their research showed that the gradient mesh structure was conducive to cell adhesion, proliferation, protein synthesis and calcium deposition, and various stages of cell maturation co-existed in

different regions of the gradient mesh structure. In addition to the design of scaffolds with axially varied porosity, other porosity variation strategies have been explored. Onal et al. [23], for example, designed dense-in and dense-out graded scaffolds. Their quasi-static mechanical tests showed that the gradient could significantly affect the failure behavior. Limmahakhun et al. [24] assembled the building units with different strut sizes to achieve FGSs with both axial and radial structural gradients.

2) FGS is designed to have cells with varied sizes. Both strut size and pore size can be tailored when cell size is changed. One distinct drawback of this strategy lies in free nodes that are located at the interface between unit cells of different sizes. These imperfections may have the potential to reduce the mechanical properties of FGS. Therefore, the applicable unit cell type and zoom level are limited. Surmeneva et al. [25] fabricated triple- and double-layered Ti-6Al-4V scaffolds based on diamond unit cell and their mechanical test results showed considerable ductility.

3) FGS is designed to have varied unit cell types. The combination of multiple unit cells offers almost unlimited possibilities for FGSs. In addition, geometric parameters, such as pore size, strut diameter and porosity, can be adjusted separately. Li et al. [26], for example, combined rhombic dodecahedron and diamond unit cells and evaluated the mechanical behavior and deformation mechanisms. Zok et al. [27] established a system for the classification of truss structure types, which offered inspirations for combining different truss unit cells. Yang et al. [28] proposed CAD methods that could realize multi-morphology transition hybridization CAD designs of minimal surface porous structures. Perfect hybridization of different classes of structures, i.e., truss structure, sheet-like units and net-like units, however, still faced difficulties.

4) FGS is designed to have varied chemical compositions. Metallic biomaterials possess stiffness and strength values over wide ranges. Magnesium, Ti-6Al-4V and 316 L stainless steel, for example, have elastic moduli of 38, 110 and 210 GPa, respectively [29]. A porous structure with a desired gradient in mechanical properties

can be achieved by combining multiple materials at a certain ratio. However, this method puts forward a high demand for the control and mechanical system in FGS fabrication.

Among the design strategies described above and shown in Fig. 1, varying strut diameter stands out in a crowd with respect to feasibility and design simplicity. Some practical problems, such as mismatching nodes and abrupt transition, can be avoided in the design and fabrication of FGS. Therefore, varying strut diameter has been extensively adopted by most of researchers to realize FGSs.

Diamond unit cell has been most commonly used to construct polyhedron structures in BTE scaffold design. It is isotropic and consists of 16 struts; every two struts intersect at an angle of 109.5°. All struts are subjected to the same bearing condition when compressive stresses are applied. Therefore, deformation is evenly distributed and the risk associated with stress concentration is minimum. Moreover, the angle between the building direction and each strut is often tuned to the same value (54.5°) in order to improve manufacturing stability and achieve a high dimensional accuracy. Furthermore, the diamond structure is very similar to the cancellous bone structure in that the inter-trabecular angle distribution of nodes with 4 connecting trabeculae has a mean value close to 109° [30]. In addition, diamond cells constitute an open mesh construction that facilitates mass transportation and communications between cells. The advantages mentioned above make the diamond unit cell an appropriate choice for constructing FGSs.

It is worth noting that most of the FGSs designed in the studies mentioned earlier were obtained by using one of the following two methods: (i) assembling unit cells with different porosities directly and (ii) varying strut diameter linearly and uniaxially. There have been few studies focusing on the effect of porosity variation strategy on the mechanical behavior and failure mechanisms of FGSs. The present study aimed at devising an effective porosity variation strategy to realize optimum permeability, elastic modulus and strength of FGS. For this purpose, six porosity variation strategies were adopted to construct the geometry models of FGSs with the aid of a self-

developed Python script. Rational designs enabled smooth transitions from the low porosity region (mimicking cortical bone) to the high porosity region (mimicking cancellous bone). Permeability tests and quasi-static mechanical tests were performed to evaluate the mechanical properties and permeability of the designed and fabricated FGSs. The Digital Image Correlation (DIC) technology was applied to monitor the deformation and failure of these FGSs during compression tests. Finally, a relationship between porosity variation strategy and the overall performance of scaffolds was established.

2. Material and methods

2.1 Design and manufacturing of FGSs

To establish the geometry models of scaffolds with varying porosity, a Python script was developed. The structure transition in FGS was controlled by the porosity equation that will be given below. The geometry models of FGSs were established using ABAQUS by importing the self-developed Python script, and STL files were subsequently exported for additive manufacturing. According to the ISO 13314 standard, the width of a rectangular specimen should be at least 10 times the average pore size and no less than 10 mm, and the ratio of specimen height to edge length should be between 1 and 2. In this study, the length of every unit cell was 1 mm, and the external dimensions of the samples were 10×10×15 mm (Fig. 2a).

Six types of scaffolds with different porosity variations were designed, namely Lin, Exp, Sigk0.5b8, Sigk1b5, Sigk1b8 and Sigk1b11. As shown in Fig. 2b, the porosities of the designed FGSs were transited from 38% (mimicking cortical bone) to 75% (mimicking cancellous bone) along the height of the sample. These graded lattice structures all possessed a highly porous outer layer to reduce the overall implant stiffness and allow extensive bone ingrowth. Gradual structure transition avoids abrupt changes at the interfaces and would benefit tissue ingrowth and mineralization [19]. In the first type of FGS, named Lin design, porosity varied linearly at a given gradient. The second type of FGS, named Exp design, possessed porosities varying exponentially and offered a larger volume

fraction of low porosity region as compared with the Lin design. The porosities of samples Lin and Exp are defined by Eqs. 1 and 2, respectively:

$$p_L(x,y,z) = Ax + By + Cz + D \tag{1}$$

$$p_E(x,y,z) = ae^{Ax+By+Cz} + b \tag{2}$$

The parameters used in the porosity control equations are listed in Table 1. With regard to samples Sigk*b*, a sigmoid function was adopted to control the structural variation and porosity gradient boundary position. The porosity of a scaffold designed with the sigmoid-function-based porosity variation strategy is defined by Eq. 3:

$$p_S\,(x,y,z) = \frac{1}{1+e^{-k*B(x,y,z)}}\rho_1 + (1 - \frac{1}{1+e^{-k*B(x,y,z)}})\rho_2 \tag{3}$$

where *k* is the control parameter of porosity variation gradient and *B(x,y,z)* the variation boundary function that is used to intersect two different porosities. A linear equation *B(x,y,z)* = *z*-*b* was used in this study to form a linear-shape boundary and the planar boundary was located at *z*=*b*. Therefore, samples Sigk0.5b8 and Sigk1b8 had the porosity gradients of *k*=0.5 and *k*=1, respectively. Sigk1b5, Sigk1b8 and Sigk1b11 possessed porosity boundaries at *z*=5, 8 and 11 mm, respectively. Designed according to the method described above, six types of scaffolds with different porosity variation strategies along the sample height are showed in Fig. 2c.

The porosity variation strategies adopted here were based on multiple considerations. The linear variation of strut thickness - a classic approach to achieving FGS, was adopted in the design of sample Lin in the present study. This strategy offers gradual variations of porosity and morphology. In the case of sample Exp, the exponential structure gradient provides a large proportion of high density structure and a rapid transition from the low porosity region to the high porosity region. A similar structural feature can be found in the natural bone tissue, such as femur mid-diaphysis, where the fraction ratio of cortical bone is higher than that of trabecular bone. An S-type function, named sigmoid function, was introduced in the design of samples Sigk*b* in order to enhance the flexibility and

simplicity of FGS design. This design can be adopted in scaffolds with a complex porosity variation boundary such as hip implant.

For comparison purposes, two sample groups P1 and P2 with uniform lattice structures were designed and fabricated. Their morphometric parameters are given in Table A1 (appendix).

The FGSs were additively manufactured by means of selective laser melting (SLM) using a 3D Systems AM250 machine from Renishaw. A grade 23 Ti-6Al-4V ELI (extra low interstitial) powder was used as the starting material. The details of SLM process parameters are given in Table 2.

2.2 Characterization of FGS morphology

The morphologies of additively manufactured FGS samples were characterized by using scanning electron microscopy (SEM) and micro-computed tomography (micro-CT). Their average density values were determined by dry weighing. Prior to dry weighing, all the FGSs samples were cleaned using an ultrasonic cleaning machine and dried. The theoretical density of the Ti-6Al-4V alloy was assumed to be 4.43 g/cm^3 and the density value of each sample was calculated by dividing its mass by the mass of a solid cuboid with the same outline dimensions. The surface morphology and fracture surface were observed using SEM (FEI Quanta 200 FEG). For imaging with the electron backscattered diffraction (EBSD) technique, samples were first ground using 600-grit, 1200-grit, 1600-grit and 2000-grit papers and then electrochemically polished. TESCAN MIRA 3LMH SEM was used. The acceleration voltage was set at 20 kV and collection frequency 20.4 Hz. EBSD data was analyzed by using the HKL channel 5 software.

The micro-CT characterization was performed by using an industrial high-resolution CT and a Phoenix nanotom m system (General Electric). The applied voltage and current were 100 kV and 135 μA, respectively. Voxel sizes of 7×7×7 μm were used to capture the details of the surface morphology of each of FGS samples. Scan time was set at 9 min in order to obtain sufficient structure information of the whole sample. 2D images of the

sample were reconstructed by using built-in software and then 2D slices were exported in the TIFF format. The image processing software ImageJ was used to perform the preprocessing of 2D cross-section images. First, the image sequence was imported and brightness/contrast was adjusted to get the crisp outline of the sample. The Bernsen method was employed in auto local thresholding, and despeckle filtering and outlier removal were performed to filter off the speckle and impulse noise. The effective calculation area was defined by the ROI manager. Finally, the geometric parameters of the FGSs, such as strut size and pore size, were calculated using the BoneJ software.

2.3 Heat treatment of FGSs

In order to check where there was under-treatment or over-treatment caused by the differences in the initial microstructures of the SLM FGSs, the microstructures of samples with varied strut thicknesses were observed using SEM and EBSD. The results, shown in Fig. 3, indicated that the morphologies of acicular martensite in these samples varied little with porosity and the lamella widths fell into a range of 430-530 μm. Therefore, it was considered reasonable to perform heat treatment for all FGS samples under the identical condition.

Based on the results of our previous research on the SLM bulk Ti-6Al-4V material [31], 900°C/2h/furnace cooling was selected as the post heat treatment scheme for the FGSs in order to improve their ductility at a minimum loss of strength. All the FGS samples were heated to 900 °C at a heating rate of 10 °C/min and held for 2 h, and then cooled inside a tube furnace.

2.4 Permeability tests of FGSs

The falling head method was used to determine the permeability of the FGSs. The experimental setup is illustrated in Fig. 4. The apparatus was mainly composed of three parts: a standpipe, a permeability chamber and a reservoir. The volume of water flowed through an FGS sample was measured by recording the initial height L_1 at $t = t_0$ and the final height L_2 at $t = t_i$. For each test, the values of L_1 and L_2 were kept the same to simplify the calculation

procedure. The hydraulic conductivity (K) of the sample was calculated from the equation of Darcy's law:

$$v = Ki \tag{4}$$

where v is the fluid velocity, K the hydraulic conductivity and i the hydraulic gradient and described by Eq. 5:

$$i = \frac{L_1 - L_2}{H} \tag{5}$$

where H is the height of FGS sample. K can be obtained by integrating water flow rate over measurement time t_i - t_0, as shown in Eq. 6.

$$K = \frac{aH}{A(t_i - t_0)} \ln\left(\frac{L_1}{L_2}\right) \tag{6}$$

where a is the cross section area of standpipe and A the cross section area of FGS sample. Based on the calculations using the equations above, the permeability k of the tested sample can be derived by applying Eq. 7.

$$k = \frac{K\mu}{\rho g} \tag{7}$$

where μ is the dynamic viscosity coefficient of water and ρ the density of water. The parameter values used to arrive at k values are listed in Table 3.

Measurements were repeated five times for every sample, resulting in fifteen measurements for each type of porosity transition.

2.5 Quasi-static mechanical testing of FGSs

Compression tests were performed using a universal material testing machine. According to the standard ISO 13314 for compression test of porous and cellular metals, strain rate was set at 3.3×10^{-3} s^{-1}. The engineering strain ε of the specimen was derived from the displacement of the crosshead of the testing machine. All the specimens were compressed to a large strain ($\varepsilon > 0.6$) so as to investigate the effect of heightwise porosity gradient on the quasi-static mechanical properties. Three specimens with a specific porosity transition was tested and no lubricant was applied at the top and bottom surfaces. Young's modulus was determined from the slope of the fitted straight line in the elastic regime. Yield strength was determined by the intersection of the stress-strain curve and a line parallel to

the linear quasi-elastic curve at a strain offset of 0.2%.

To minitor the deformation and failure modes during the compression tests, the digital image correlation (DIC) technology was applied to register the compression deformation of the specimen. Before the compression test, one side face of the specimen was painted to have a white backgroud and then speckled with black paint to increase image contrast. A 2D DIC system NCM-2D 2016 was used. The compression test was monitored by two high-resolution CCD (couple-charged device) cameras. Collection frequency was set at 5 Hz. The displacement contour along the specimen height was analyzed using the build-in software.

In addtion , compression tests of specimens P1 and P2 with uniform lattice structures (Table A1) were conducted with the aid of DIC to compare their deformation behavior and failure mode with those of FGS specimens.

2.6 Statistical analysis

The SPSS statistics software (IBM Statistics SPSS 22) was used to calculate the *p* value and to find statistically significant differences. The results were presented as mean ± deviations. Comparison was made with the one-way analysis of variance (ANOVA), followed by performing Tukey's test. A *p* value of less than 0.05 was considered statistically significant.

3. Results

3.1 Average densities and morphologies of the FGSs

The average mass varied from 3.043 g (Sigk1b5) to 4.111 g (Sigk1b11) due to different porosity transition modes and varied locations of the transition boundary of samples Sigk*b*. The average porosities of the samples ranged from 40.9% (Sigk1b11) to 55.8% (Sigk1b5). According to the CAD designs, the value of porosity increased from 38% in the densest region to 75% in the most porous region. It was found that the as-built samples were all heavier and possessed slightly lower average porosities than the designed structures (Fig. 5). The diviations were

considered to be caused by (i) particle attachment to strut surfaces during SLM and (ii) large layer thickness (50 μm). For a given angle included between the building direction and strut axis, the surface roughness of strut increases with increasing layer thickness.

The topographic features of the FGSs, revealed by SEM, are shown in Fig. 6. A distinct phenonmenon of partical attachment to strut surfaces was observed. The observation could explain the results obtained from the dry weighing tests that the as-built samples were all heavier than the values expected from the designs (Fig. 5). The heightwise graded porous structures could be easily observed from the sideview given in Fig. 6. Gray scale images captured by micro-CT revealed the clear outlines on the cross sections of sample Sigk1b8. In addition, micro-CT analysis confirmed the interconnectivity of pores in the as-built FGSs.

The variations of strut diameter and pore size along the sample height are shown in Figs. 7 and 8, respectively. The geometric parameters of the FGSs are also summaried in Table A2 (appendix). All the CAD design structures started with a strut diameter of 475 μm and a pore size of 225 μm at the bottom and ended with a strut diameter of 250 μm and a pore size of 450 μm at the top. The actual strut diameter values of the as-built samples were 0~35 μm larger than the design values, while the pore size values of the as-built samples were 0~55 μm smaller than those of the CAD design structures. Despite these deviations, both strut diameters and pore sizes of the as-built samples clearly reflected the transition characteristics of each of the porosity variation strategies. The strut diameter and pore size of sample Lin, for example, varied linearly from 486 to 270 μm and from 180 to 390 μm, respectively. In the case of sample Exp, the strut diameter and pore size changed moderately over a height of 8~9 mm from the bottom and then the strut diameter and pore size changed rapidly to 273 and 430 μm over a height of 10~15 mm from the bottom, respectively. A samller structure gradient was obtained in sample Sigk0.5b8, as compared with sample Sigk1b8. Over a sample height of 6 to 8 mm, the strut diameters of Sigk0.5b8 and Sigk1b8 decreased by 25.3 and 32.8%, respectively. The median gradient points of samples Sigk1b5, Sigk0.5k8, Sigk1b8 and Sigb1b11

were located at heights of 5.2, 8.8, 8.8 and 10.7 mm above the bottom of the FGSs and good agreements with design values were achieved. Samples Exp and Sigk1b11 possessed large proportions of the low porosity structure (i.e., a porosity of 38% - design value), while sample Sigk1b5 contained the largest volume of the high porosity structure (i.e., a porosity of 75% - design value). The results further indicated that the strut diameters and pore sizes of the as-built samples had similar gradient features to the CAD design counterparts.

To present a comprehensive view of the distributions of the geometric parameters of the as-built samples, the strut diameters and pore sizes in the regions with different porosities were calculated and six samples were compared (Fig. 9). It can be seen from the scatterred data points that the strut diameters of the as-built samples are all larger than the design values, indicating a marked strut thickening effect during SLM. In further research, layer thickness, laser power and hatching space should be optimized to minimize the deviations in strut diameter and pore size from design values, together with the considerations on the effects of changing these parameters on build speed, microporosity, microstructure and mechanical properties.

3.2 Permeability of the FGSs

The measured permeability values plotted against the average porosity are shown in Fig. 10 and Table A2. In general, for a given sample, the higher the average porosity, the higher the permeability. However, the permeability values did not increase systematically with increasing average porosity - a result being different from the findings of other researchers concerning the scaffolds with uniform porosity [32, 33]. This result indicated that porosity variation strategy could indeed strongly affect the permeability of FGS in a unique way. The highest (0.491×10^{-9} m^2) and lowest (0.129×10^{-9} m^2) permeability values were found for samples Sigk1b8 and Sigk1b11, respectively.

3.3 Mechanical properties of the FGSs

A typical engineering stress-strain curve of FGS is shown. It can be divided into three stages: elastic stage, quasi-plateau stage and densification stage (Fig. 11). Young's modulus (E_s), yield strength (σ_s), first peak stress (σ_{1th}) and

quasi-plateau stress (σ_{pl}) were determined from the curves shown in Fig. 12. It should be noted that the plateau stage appeared to show an ascending trend instead of being dynamically stable over a specific range of strains [34], which was obviously caused by increasing overall density along the specimen height. In this case, the quasi-plateau stress σ_{pl} was determined by the arithmetical mean of the stresses between strains of 5% and 20%.

With regard to the as-built specimens (Fig. 12), the axial gradient structures of samples Exp, Sigk0.5b8 and Sigk1b11 dramatically raised the curves at the quasi-plateau stage and showed a significant effect of densification, as compared with those of samples Sigk1b5, Sigk1b8 and Lin. Heat treatment apparently reduced the fluctuations of the stress-strain curves of samples Sigk1b5, Sigk1b8 and Lin, corresponding to a gradual failure process.

As shown in Fig. 13a and Table A2 (appendix), the Young's moduli of the as-built samples varied between 3.3 (Sigk1b5) and 5.2 GPa (Sigk1b11), and E_{s} of the as-heat-treated samples ranged from 3.5 (Sigk1b5) to 5.7 GPa (Sigk1b11). The Young's modulus showed a positive correlation with the average porosity (Fig. 14a). The yield strength σ_{s} ranged between 60.94 (Sigk1b5) and 84.69 MPa (Sigk0.5b8) for the as-built samples. The heat treatment applied significantly reduced the strengths of the samples, leading to a strength range from 27.09 (Sigk1b5) to 65.37 MPa (Sigk1b11), as shown in Fig. 13b and Table A2. However, σ_{s} showed no correlation with the average porosity (Fig. 14b). Sample Sigk0.5b8 possessed the highest strength-weight ratio as compared with the samples of other designs. The first peak stresses of the FGSs were slightly higher than the yield strengths (Fig. 14c and Table A2) for both the as-built and as-heat-treated samples, indicating that yielding was immediately followed by structure failure and the improvements in the plasticity of the FGSs through the heat treatment were rather limited.

Porosity variation strategy showed a significant influence on the quasi-plateau stresses of the FGSs (Fig. 13d and Table A2). The stress-strain curve entered the densification stage when the compressive strain reached 0.2 and the stress dramatically increased at this stage for both the as-built and as-heat-treated samples. Sample Exp showed

the highest value (222.07 MPa for the as-built samples and 145.99 MPa for the as-heat-treated samples), which were about five times of the values of sample Sigk1b5. The samples with the same transition midpoint position (H=8 mm), i.e., samples Lin, Sigk0.5b8 and Sigk1b8, could be ranked according to the σ_{pl} values: Sigk0.5b8 > Lin > Sigk1b8. The heat treatment did not change the order of σ_{pl} values. A steadily rising trend of stress-strain curve was observed for the FGSs, especially for samples Exp, Sigk0.5b8 and Sigk1b11, indicating increasing deformation resistance with rising strain and great fracture toughness.

It is generally observed that a uniaxially compressed bulk metallic specimen possesses a deformation gradient in the loading direction, meaning that the height-wise deformation speed gradually decreases from the top (testing speed) to the bottom (zero) and remains unchanged on the same horizontal plane during the test. The deformation mechanism of a compressed FGS is, however, significantly different from that of a typical bulk specimen, as shown in Fig. 15.

Fig. A1 and Fig. 15 show the vertical displacement distributions of compressed specimens with uniform lattice structures and FGS specimens captured by CCD cameras, respectively. The typical deformation phases of the specimens during the compression tests are presented column by column. At the same deformation phase, the deformation characteristics of the specimens are compared between rows. At the initial stage of the contact between the crosshead and specimen, the vertical (heightwise) displacement (d_v) was distributed in the specimen with a distinct horizontal gradient, but almost uniformly along its height. This horizontal gradient was because the top surface of the specimen was not strictly horizontal so that the crosshead contacted the higher side first and a greater vertical displacement occurred on this side. As the compression test proceeded further, the specimen started to deform elastically and the gradient direction of displacement d_v quickly shifted to the quasi-diagonal, which indicated that elastic shear deformation occurred. In the regions where the displacement gradient d_v was evenly distributed, the angle (α_s) between the direction of the displacement gradient d_v and horizontal plane could be

calculated (see the column “Elastic stage” in Fig. 15). Specimens with uniform lattice structures followed a 45° inclined deformation mode from the top to the bottom, as shown in Fig. A1, whereas FGS specimens changed the deformation mechanism by either increasing the deformation angle of the upper portion (Exp and Sigk1b11) or decreasing the deformation angle of the lower portion (Sigk0.5b8, Sigk1b5 and Sigk1b8). For samples Lin, Sigk0.5b8, Sigk1b5 and Sigk1b8, the α_s values fluctuated around 45°, which were significantly smaller than those of samples Exp (55.2°) and Sigk1b11 (55.9°). The differences in deformation angle can be explained by the fact that the denser part has higher stiffness and does not deform easily. It is worth noting that samples Exp and Sigk1b11 also possessed relatively higher Young’s moduli than the other samples. This result manifested that the mechanical properties of FGS are closely related to its deformation mechanism.

Large failure planes were formed in specimens with uniform lattice structures after the 1st load dropping (Fig. A1), indicating severe fracture failure after yielding. For the FGSs, however, yielding occurred at the end of the elastic stage and struts with a smaller diameter fractured first and a quasi-layerwise failure occurred. The first stress reduction caused by the failure of struts took place shortly after yielding, as can be observed in Fig. 15 (see the column “1st load dropping”). A displacement concentration area (i.e., the regions in the orange and red colors) close to the crosshead shrank. Except for sample Sigk1b5 whose failure occurred near the transition boundary (k=5 mm), failure was associated with the local vulnerable area rather than the overall graded structure, which is consistent with the result showed in Fig. 14b. Furthermore, a large proportion of the highly porous structure indeed increased the risk of yielding and failure, as confirmed by the results of Sigk1b5 and shown in Fig. 13b and c. Generally, the directions of displacement gradient d_v of the upper part of all FGS specimens tended to be vertical. This transition was considered to be caused by the redistribution of d_v after the 1st load dropping.

The failure process was recorded by CCD cameras. At the densification stage, specimens with uniform lattice structures experienced fracture failure repeatedly and multi-failure planes were formed, as shown in Fig. A1 a and

b. The severe damage caused the vibrations of specimens and, as a result, the DIC system failed to track the pixels. Different failure mechanisms of the FGSs can be observed in Fig. 15 (see the column “densifying stage”). One or more failure planes that occurred at an angle of 45° with the horizontal plane were detected in samples Lin, Exp and Sigk1b11 (outlined by red lines in Fig. 15). Samples Exp and Sigk1b11 showed significantly stronger deformation resistance at this stage (Fig. 13d). Sigk0.5b8, Sigk1b5 and Sigk1b8 showed quite moderate failure behaviors with no typical shear failure plane occurring until the compressive strain reached 0.6. A large proportion of the low porosity region could increase the deformation resistance at the densification stage and lead to the generation of a 45° inclined failure plane (Exp and Sigk1b11 in Fig. 15 - the column “densifying stage”). Sigmoid function-controlled porosity gradient not only made the densification process more stable but also enhanced the deformation resistance by tuning the gradient parameter k properly (Sigk0.5b8 in Fig. 13d).

The material retention ratio r of specimen can be defined as M_c/M_i, where M_c is the mass of the compressed specimen and M_i the mass of the original specimen. A higher r value indicates a greater capability of withstanding large deformation while maintaining the structural integrity of the porous biomaterial. It can be found that the r values of all compressed FGS specimens exceeded 85% (Fig. 16a). The axial porosity gradient designs largely maintained the plastic deformation capacities of the FGSs without generating any large fragments. The heat treatment showed a great effect on the morphology of fracture surface. In general, the as-built samples possessed both dimple fracture features (Fig. 16b and c) and river-like fracture features (Fig. 16b and d), indicating the involvement of brittle fracture. However, the as-heat-treated samples showed the typical feature of intergranular fracture and a coarse lamellae fracture morphology could be easily observed (Fig. 16e and f).

4. Discussion

In this study, Ti-6Al-4V FGSs with six types of heightwise transition porosities were additively manufactured, characterized and tested. In general, the characteristic morphology, permeability and mechanical behavior of the

FGSs based on diamond unit cell reflected their structural features, especially the mode of porosity transition. The study provided basic knowledge for the design of FGS and an insight into the transition boundary design between the regions with high porosity and low porosity.

4.1 Morphological characteristics of the FGSs

Complex porosity-graded structure presents a challenge for its fabrication using SLM, because many factors, such as strut thickness, the angle between the strut and building direction, all have marked impacts on the resultant FGS [35]. One important advantage of FGSs based on diamond unit cell lies in strut size stability during SLM, because all struts have an identical angle of 54.7° with the building direction [34]. In the present study, the FGSs fabricated by SLM covered a wide range of porosities (38%~75%), strut diameters (253~516 μm) and pore sizes (180~460 μm). The results of morphological characterization demonstrated that the geometric dimensions of the as-built samples were in good agreement with the design values. Deviations in strut diameter and pore size remained fairly stable along the height of the FGSs. It was also observed that an FGS with a large structural gradient is more prone to fracture, partly due to significant residual stresses caused by rapid dimensional changes in strut diameter. Obviously, the minimum strut diameter cannot go beyond the minimum 3D printable structure features which is set by the SLM technology [7]. In this study, the minimum 3D-printable strut diameter was found to be 250 μm (porosity=75%, unit size=1 mm). Each of the porosity variation strategies chosen could serve the purpose of creating FGS with porosity changing from the low porosity region (properties close to cortical bone) to the high porosity region (properties close to cancellous bone), as confirmed by the results of micro-CT tests (Figs. 7, 8 and 9). In other words, both the choice of the type of unit cell and the dimensional variation of FGS struts are of great importance.

It is worthwhile to note that all the as-built samples showed an effect of strut swelling (Fig. 7). Generally, strut diameter was about 30 μm thicker than the design value, which is very close to the average particle size of the Ti-

6Al-4V powder used (33.1 μm), indicating that powder particle attachment to strut surface was the main contributor. In addition, coarse surfaces of struts contributed to significant pore size deviations (Fig. 8).

The FGSs designed and investigated in this study satisfied the specific requirement of connecting the cortical bone scaffold and trabecular bone scaffold. When the morphological features of the FGS's in the highly porous region (350 μm <pore size<450 μm, 250 μm <strut diameter<350 μm, 56.5%< porosity <75%) and those in the study of Goulet et al. (320 μm < trabecular plate separation <1670 μm, 64%< bone volume fraction) [36] are compared, it can be found that the key morphometric parameters are in agreement with those of natural human bone. The low porosity region (38%<porosity<56.5%), which was intended to link the low porosity scaffold and cortical bone, is well connected with the high porosity region through different transition structures. This interconnected porous structure guarantees the satisfaction of the biological property requirements of BTE scaffolds and offers diversity in mechanical properties. The sigmoid function showed a distinct controllability over the transition boundary, as the samples adopting the sigmoid function in porosity transition had a shorter transition segment length compared with the other designs. With regard to samples Sigk1b5, Sigk1b8 and Sigk1b11, strut diameter had a smooth reduction of 150 μm over a length of 5 mm, offering an insight into transition structure design possibilities for FGS.

Generally, the anatomy of natural bone is functionally graded. This is caused by the requirements to maximize the stiffness and strength in the main loading direction, while keeping minimum bone mass. Truss structure based on the combination of struts contains a large number of join nodes, which offers a rich diversity to unit cell type [27]. Functionally graded structures can be easily obtained by adding or subtracting struts in Element Pro (nTopology) or other modeling software. Moreover, STL files of the FGSs generated by the Python script in the present study have relatively small file sizes of 20~30 MB, making them convenient to be handled by any additive manufacturing system.

4.2 Effect of graded porosity on the permeability of the FGSs

In the present study, the measured permeability did not show a unique correlation with the average porosity, which is inconsistent with the findings of other researchers with regard to uniform porous structures [32, 37-39]. This inconsistency is believed to be caused by the combination of different porosities in the diamond unit cell based FGSs. The volume fraction of the high porosity region plays a crucial role in enhancing the permeability of the diamond unit cell based FGSs. Samples Sigk0.5b8, Sigk1b5 and Sigk1b8 with relatively lower masses showed higher permeability values (4.91×10^{-10}, 4.82×10^{-10} and 4.08×10^{-10} m^2, respectively) than the samples of other designs. This can be explained by the fact that samples Sigk0.5b8, Sigk1b5 and Sigk1b8 possessed a larger portion of high porosity region than the other samples, which provided sufficient water flow and routed water into the low porosity region. A large volume fraction of high porosity region helps increase the water flow rate in the denser region [40]. It was noticed that the permeability values of the FGSs overlapped with those of human proximal tibia [37]. Compared with the scaffolds with similar average porosities (40~50%) used in other studies (Table 4), the FGS samples with sigmoid function-controlled boundaries showed comparable permeability values. For a specific transition segment length, the sigmoid function appears to be a flexible function to adjust the porosity gradient. It can be concluded that by adopting a proper transition boundary controlling strategy, the requirements of transferring nutrients and oxygen from the bone tissue to the scaffold and providing sufficient mechanical support can be met simultaneously.

4.3 Compressive behavior of the FGSs

The slopes of the quasi-elastic part of the fitted stress-strain curves were taken to be the Young's moduli of the FGSs with porosity variations from 75% (top) to 38% (bottom). The Young's moduli of the as-built samples varied from 3.3 to 5.7 GPa, being close to those of the as-heat-treated samples (between 3.5 and 5.2 GPa), and overlapped with the Young's moduli of trabecular bone (0.1 – 4.5GPa) [41] and cortical bone (3-20 GPa) [42]. The porosity-

graded scaffolds showed a potential of replacing natural bone in different areas with varying bone densities. Such graded structures can be used as a hybridization of cancellous bone scaffold and cortical bone scaffold. The measured Young's moduli showed a positive correlation with the average porosity (Fig. 14a) and the results of other studies also proved that the Young's modulus was closely related to the volume fractions of structures with different porosities [34, 43-45]. These findings provided guidelines for evaluating and predicting the Young's modulus of FGS. However, marked deviations were found from the predictions of Young's modulus made on the basis of established analytical relationships [46], which could be caused by the deviations in strut diameter and porosity from the design values and also by structural defects present inside the SLM FGSs.

The porous scaffold with diamond cells is thought to be a bending-dominated structure and each unit cell consists of 16 struts and 8 (4+6×1/2+4×1/4) frictionless joints, satisfying Maxwell's criterion of M = b-3j+6=16-3×8+6=-2<0. This structure is unstable under compressive stresses and tends to reach another stable state. The struts of diamond unit cell are parallel with the plane that forms an angle of 45° with the cross section of the sample. Out-of-plane bending occurred when the scaffold was subjected to compressive stress, resulting in 45° shear deformation, as confirmed by the vertical displacement contour shown in Fig. 15. The angles between the gradient direction of d_v and the cross-section of samples Lin, Sigk0.5b8, Sigb1b5 and Sigk1b8 are 43.9°, 46.7°, 45.4° and 45.0°, respectively. This deformation mechanism is in line with the prediction of Kadkhodapour et al. [47]. One interesting finding is that for samples Exp and Sigk1b11, the shear deformation angle increased to values larger than 55°. Given the fact that both of these samples have large volume fractions of the high density structure, it can be concluded that the low porosity part provided a stiff support and thus reduced the deflection of the upper part. Therefore, changing stiffness brought about by the gradient structure indeed affects the deformation mechanism of the scaffold. The shear deformation angle can be modified by changing the structural gradient of FGS.

Cortical bone plays an important role in supporting the whole body weight and has a high stiffness value ranging from 5-23 GPa [48]. Thus, the feature of high stiffness cannot be overlooked in developing load-bearing scaffolds. Metallic porous scaffolds are generally thought to be appropriate choices as load-bearing implants. However, considering the biological requirements for cell attachment, proliferation and growth, most of metallic scaffolds studied have been designed to have high porosities and large pore sizes, leading to relatively low Young's moduli [34, 44, 47, 49]. This plight can be alleviated by FGS that has sufficient stiffness at a proper location and allows unimpeded mass transport within the whole scaffold through interconnected pores. In the present study, the rationally designed structures provided the FGSs with favorable stiffness for cortical and cancellous-cortical bone replacement as well as sufficient space for tissue regeneration.

The yield strengths of the as-built and as-heat-treated FGSs varied from 60.94 to 84.69 MPa and 27.09 to 65.37 MPa, respectively. The measured values fall into the range of the strengths of cortical bone [47]. All structure failures of the FGSs initiated in the highly porous region - a result consistent with the findings of Onal et al. [23]. Thus, the highly porous region of FGS should be rationally designed to prevent premature failure. The yield strength values of samples Lin, Exp, Sigk0.5b8, and Sigk1b11 are generally higher than those of samples Sigk1b5 and Sigk1b8. The gradient variation of the highly porous structure in the FGSs could be the root cause for the differences. With regard to samples Lin, Exp, Sigk0.5b8 and Sigk1b11, their strut diameters increased to various extents over a height of approximately 3 mm (below the crosshead) and thus compressive stress could be efficiently transferred to the part of the structure with thicker struts. Compared with Young's modulus, yield strength is more closely related to the local structure change in FGS, which can be proven by Fig 14b. This explanation is applicable also to the as-heat-treated samples.

The analytical relationships established to predict the yield strengths of open cell structures were found to grossly overestimate the yield strengths of axially graded structures [46], indicating the inapplicability of these

relationships and the need to develop valid ones specific for FGSs.

First load dropping occurred shortly after yielding, followed by quasi-layerwise failure. Being different from the failure planes inclined at 45° across multiple layers of unit cells, as observed in other studies [22, 45], in the present study, the failure plane was composed of a series of small 45° inclined planes that were restricted to one or two layers of unit cells, as can be observed from the vertical displacement contour in Fig. 15 (column "1st load dropping"). Compressive stress was effectively transmitted downwards and structure failure along the sample height was avoided.

A significant influence of porosity variation strategy on the failure mechanism at the densification stage was captured by CCD cameras. The self-developed STL generating script offered great freedom in FGS design, and each strut diameter varied according to its coordinate in 3D space. The sigmoid function significantly moderated the densification process. Being different from the 45° inclined failure plane observed in other studies on scaffolds with bending-dominated structures [50, 51] and severe fracture failure of the control groups P1 and P2, the sigmoid function controlled FGSs showed stable gradual failure without generating large fragments. Even at the densification stage, no sign of large-scale shear failure across several unit cell layers was detected. The structural integrity of the FGSs was retained. The sigmoid porosity variation strategy effectively avoided intense destruction and shortened the transition segment length of the FGSs.

SLM metallic scaffolds are often subjected to compressive stresses during their service life. A crash may lead to sudden failure of bone scaffold and large-scale fragments may lead to secondary injury to the human body. The FGSs showed a favorable combination of transition segment length, material retention ratio and stable gradual failure mechanism. The results indicated that the FGSs with high material retention ratios may be squashed without large-scale fragments. A gradual failure mechanism of the FSGs can effectively prevent the generation of loose scaffold fragments and thereby reduce the risk of inflammation and repeated surgeries.

It should be noted that the heat treatment brought about significant changes to the fracture surface. During the heat treatment, the initial acicular α′ phase was decomposed to lamellar α and β phases, and the β phase was a softer phase and promoted the growth of micro cracks at the early stage of failure. The relative sizes of lamellae width and strut diameter generate a scale effect; the larger the lamellae size, the easier the strut becomes fractured. Although the heat treatment can make deformation more moderate and reduce stress fluctuations, the scale effect of α+β lamellae cannot be overlooked in the post-treatment of FGS.

4.4 Some implications of FGS design

The biological and mechanical properties of FGS can be adjusted by tuning its geometric parameters, such as strut diameter and pore size. This study has laid out a highly efficient method for generating FGSs based on the given porosity variation equations. The shape of transition boundary and the porosity gradient can be defined by mathematical equations. The script-based design method for FGSs greatly facilitates the parametric designs. A rich set of unit cell library can further be embedded into the script to mimic complex and spatially changing structures of natural bone tissue better.

Porosity variation strategy has been proven to have a significant effect on the deformation and failure mechanisms. This outcome implies that designers can not only adjust the quasi-static properties of FGS by changing the porosity variation strategy but also make the FGS well attached to the adjacent tissue during deformation and avoid abrupt failure even after crash. More research is needed to capitalize on these notable features of the FGSs and characterize their in-vitro and in-vivo behavior further.

5. Conclusions

To determine the effect of functionally graded structure on the permeability and mechanical properties of scaffolds for bone tissue engineering, Ti-6Al-4V FGSs with varying porosity along the height were designed and fabricated

by means of SLM. The morphology, permeability and mechanical properties of the FGSs were characterized by using micro-CT, the falling head method and compression tests, respectively. The DIC technology was adopted to monitor deformation during compression tests. Comparisons between the FGSs designed with six different porosity variation strategies led to the following conclusions.

(1) The Python script developed showed a great capacity of designing FGSs with diamond unit cells, pore size variation between 250~450 μm, strut diameter variation between 225~475 μm and structure transitions following linear, exponential and sigmoid functions. The sigmoid function could flexibly control the gradient and location of porosity transition boundary.

(2) Compression tests revealed that porosity variation strategy had a marked impact on the mechanical performance of FGS samples. The Young's moduli (3.3~5.7 GPa) and yield strengths (27.1~84.7 MPa) of all the FGSs fell into the ranges of cancellous bone and cortical bone, which suggested that the use of these designs as the transitions for trabecular bone scaffold and cortical bone scaffold could be considered. Young's modulus showed a positive correlation with the average density of the FGS. In contrast to the yielding behavior of scaffolds with uniform porosity, the FGSs showed a quasi-layerwise yielding behavior. The heat treatment applied significantly reduced the yield strength by 15~56%. Among the FGSs, sample Sigk0.5b8 showed superior specific Young's modulus and strength.

(3) With the aid of CCD cameras, porosity variation strategy was proven to have a significant effect on the deformation behavior and failure mechanisms of the FGSs. The highly porous upper part of the FGSs followed a tilting deformation mode and the changing stiffness brought about by the gradient structure was proven to affect the deformation mechanism of the scaffold. The sigmoid function controlled FGSs showed a moderate layer-wise failure behavior without forming large failure planes, especially at the densification stage. The FGSs showed good structural integrity during compression tests; material retention ratios higher than 90% were obtained for samples

Sigk0.5b8 and Sigk1b8 when compressive strain reached 0.6.

(4) The permeability values of the FGSs ($0.491\times10^{-9} \sim 0.129\times10^{-9}$ m^2) overlapped with the values of natural bone reported in the literature. The FGSs Sigk0.5b8 and Sigk1b8 using the sigmoid function-controlled transition boundary showed great potential to increase the permeability and strength to weight ratio.

6. Acknowledgements

The authors (Wei Liu and Lei-Lei Xing) greatly acknowledge the financial support by the National Natural Science Foundation of China (project No. U1605243). The authors (Xiang-Yu Zhang and Gang Fang) gratefully acknowledge the partial financial support from the State Key Lab of Tribology, China (project No. SKTL2016B11).

7. Data availability statement

The raw/processed data required to reproduce these findings cannot be shared at this time due to technical or time limitations.

Appendix

The morphology parameters of samples P1 and P2 with uniform unit cells are listed in Table A1.

All the morphology parameters, permeability and mechanical properties of the samples in the present study and human bone tissue are summarized in Table A2.

The deformation behavior of samples P1 and P2 were monitored using DIC technology. The vertical displacement (d_v) distribution of uniform samples as well as the results of failure behavior observed by other researchers [23] are illustrated in Fig. A1.

References

[1] M. Liebschner, M. Wettergreen, Optimization of bone scaffold engineering for load bearing applications, Topics in Tissue Engineering, Eds. N. Ashammakhi & P. Ferretti, University of Oulu, (2003) 1-39.

https://pdfs.semanticscholar.org/f755/0eaf98f469f2ba3e13d7223d8f528f39f5a6.pdf

[2] F. Linde, I. Hvid, The effect of constraint on the mechanical behaviour of trabecular bone specimens, J. Biomech., 22 (1989) 485-490. https://doi.org/10.1016/0021-9290(89)90209-1

[3] E.F. Morgan, T.M. Keaveny, Dependence of yield strain of human trabecular bone on anatomic site, J. Biomech., 34 (2001) 569-577. https://doi.org/10.1016/S0021-9290(01)00011-2

[4] M. Niinomi, M. Nakai, J. Hieda, Development of new metallic alloys for biomedical applications, Acta Biomater., 8 (2012) 3888-3903. https://doi.org/10.1016/j.actbio.2012.06.037

[5] A.A. Zadpoor, J. Malda, Additive manufacturing of biomaterials, tissues, and organs, Ann. Biomed. Eng., 45 (2017) 1-11. http://dx.doi.org/10.1007/s10439-016-1719-y

[6] S. Limmahakhun, A. Oloyede, K. Sitthiseripratip, Y. Xiao, C. Yan, 3D-printed cellular structures for bone biomimetic implants, Addit. Manuf., 15 (2017) 93-101. https://doi.org/10.1016/j.addma.2017.03.010

[7] S. Arabnejad, R.B. Johnston, J.A. Pura, B. Singh, M. Tanzer, D. Pasini, High-strength porous biomaterials for bone replacement: A strategy to assess the interplay between cell morphology, mechanical properties, bone ingrowth and manufacturing constraints, Acta Biomater., 30 (2016) 345-356. https://doi.org/10.1016/j.actbio.2015.10.048

[8] J. Wieding, A. Jonitz, R. Bader, The effect of structural design on mechanical properties and cellular response of additive manufactured titanium scaffolds, Materials, 5 (2012) 1336-1347. http://dx.doi.org/10.3390/ma5081336

[9] M.N. Cooke, J.P. Fisher, D. Dean, C. Rimnac, A.G. Mikos, Use of stereolithography to manufacture critical‐sized 3D biodegradable scaffolds for bone ingrowth, J. Biomed. Mater. Res. B: Appl. Biomater., 64 (2003) 65-69. https://doi.org/10.1002/jbm.b.10485

[10] D.H. Kohn, M. Sarmadi, J.I. Helman, P.H. Krebsbach, Effects of pH on human bone marrow stromal cells in vitro: implications for tissue engineering of bone, J. Biomed. Mater. Res. A, 60 (2002) 292-299. https://doi.org/10.1002/jbm.10050

[11] X.-Y. Zhang, G. Fang, J. Zhou, Additively manufactured scaffolds for bone tissue engineering and the prediction of their mechanical behavior: A review, Materials, 10 (2017) 50. http://dx.doi.org/10.3390/ma10010050

[12] C. Cheah, C. Chua, K. Leong, S. Chua, Development of a tissue engineering scaffold structure library for rapid prototyping. Part 1: investigation and classification, Int. J. Adv. Manuf. Tech., 21 (2003) 291-301. https://doi.org/10.1007/s001700300034

[13] C. Cheah, C. Chua, K. Leong, S. Chua, Development of a tissue engineering scaffold structure library for rapid prototyping. Part 2: parametric library and assembly program, Int. J. Adv. Manuf. Tech., 21 (2003) 302-312. https://doi.org/10.1007/s001700300035

[14] L.J. Gibson, M.F. Ashby, Cellular solids: structure and properties, Cambridge university press, 1999. http://dx.doi.org/10.1017/CBO9781139878326

[15] R. Hedayati, S. Ahmadi, K. Lietaert, B. Pouran, Y. Li, H. Weinans, C. Rans, A. Zadpoor, Isolated and modulated effects of topology and material type on the mechanical properties of additively manufactured porous biomaterials, J. Mech. Behav. Biomed. Mater., 79 (2018) 254-263. https://doi.org/10.1016/j.jmbbm.2017.12.029

[16] S. Ahmadi, R. Hedayati, Y. Li, K. Lietaert, N. Tümer, A. Fatemi, C. Rans, B. Pouran, H. Weinans, A. Zadpoor, Fatigue performance of additively manufactured meta-biomaterials: The effects of topology and material type, Acta Biomater., 65 (2018) 292-304.

[17] R. Hedayati, H. Hosseini-Toudeshky, M. Sadighi, M. Mohammadi-Aghdam, A.A. Zadpoor, Computational prediction of the fatigue behavior of additively manufactured porous metallic biomaterials, Int. J. Fatigue, 84 (2016) 67-79. https://doi.org/10.1016/j.ijfatigue.2015.11.017

[18] X. Tan, Y. Tan, C. Chow, S. Tor, W. Yeong, Metallic powder-bed based 3D printing of cellular scaffolds for orthopaedic implants: A state-of-the-art review on manufacturing, topological design, mechanical properties and biocompatibility, Mater. Sci. Eng. C,76 (2017) 1328-1343. https://doi.org/10.1016/j.msec.2017.02.094

[19] W. van Grunsven, E. Hernandez-Nava, G.C. Reilly, R. Goodall, Fabrication and mechanical characterisation of titanium lattices with graded porosity, Metals, 4 (2014) 401-409. http://dx.doi.org/10.3390/met4030401

[20] C. Han, Y. Li, Q. Wang, S. Wen, Q. Wei, C. Yan, L. Hao, J. Liu, Y. Shi, Continuous functionally graded porous titanium scaffolds manufactured by selective laser melting for bone implants, J. Mech. Behav. Biomed. Mater., 80 (2018) 119-127. https://doi.org/10.1016/j.jmbbm.2018.01.013

[21] I. Maskery, N. Aboulkhair, A. Aremu, C. Tuck, I. Ashcroft, R.D. Wildman, R.J. Hague, A mechanical property evaluation of graded density Al-Si10-Mg lattice structures manufactured by selective laser melting, Mater. Sci. Eng. A, 670 (2016) 264-274. https://doi.org/10.1016/j.msea.2016.06.013

[22] K. Nune, A. Kumar, R. Misra, S. Li, Y. Hao, R. Yang, Functional response of osteoblasts in functionally gradient titanium alloy mesh arrays processed by 3D additive manufacturing, Colloids Surf. B. Biointerfaces, 150 (2017) 78-88. https://doi.org/10.1016/j.colsurfb.2016.09.050

[23] E. Onal, J.E. Frith, M. Jurg, X. Wu, A. Molotnikov, Mechanical Properties and In Vitro Behavior of Additively Manufactured and Functionally Graded Ti6Al4V Porous Scaffolds, Metals, 8 (2018) 200. https://doi.org/10.3390/met8040200

[24] S. Limmahakhun, A. Oloyede, K. Sitthiseripratip, Y. Xiao, C. Yan, Stiffness and strength tailoring of cobalt chromium graded cellular structures for stress-shielding reduction, Mater. & Des., 114 (2017) 633-641. https://doi.org/10.1016/j.matdes.2016.11.090

[25] M.A. Surmeneva, R.A. Surmenev, E.A. Chudinova, A. Koptioug, M.S. Tkachev, S.N. Gorodzha, L.-E. Rännar, Fabrication of multiple-layered gradient cellular metal scaffold via electron beam melting for segmental bone reconstruction, Mater. & Des., 133 (2017) 195-204. https://doi.org/10.1016/j.matdes.2017.07.059

[26] S. Li, S. Zhao, W. Hou, C. Teng, Y. Hao, Y. Li, R. Yang, R. Misra, Functionally Graded Ti-6Al-4V meshes with high strength and energy absorption, Adv. Eng. Mater., 18 (2016) 34-38. https://doi.org/10.1002/adem.201500086

[27] F.W. Zok, R.M. Latture, M.R. Begley, Periodic truss structures, J. Mech. Phys. Solids, 96 (2016) 184-203. https://doi.org/10.1016/j.jmps.2016.07.007

[28] N. Yang, Z. Quan, D. Zhang, Y. Tian, Multi-morphology transition hybridization CAD design of minimal surface porous structures for use in tissue engineering, Comput. Aided Design, 56 (2014) 11-21. https://doi.org/10.1016/j.cad.2014.06.006

[29] V. Manakari, G. Parande, M. Gupta, Selective laser melting of magnesium and magnesium alloy powders: A review, Metals, 7 (2016) 2. http://dx.doi.org/10.3390/met7010002

[30] N. Reznikov, H. Chase, Y. Ben Zvi, V. Tarle, M. Singer, V. Brumfeld, R. Shahar, S. Weiner, Inter-trabecular angle: A parameter of trabecular bone architecture in the human proximal femur that reveals underlying topological motifs, Acta Biomater., (2016). https://doi.org/10.1016/j.actbio.2016.08.040

[31] X.-Y. Zhang, G. Fang, S. Leeflang, A.J. Böttger, A.A. Zadpoor, J. Zhou, Effect of subtransus heat treatment on the microstructure and mechanical properties of additively manufactured Ti-6Al-4V alloy, J. Alloys Compd., 735 (2018) 1562-1575. https://doi.org/10.1016/j.jallcom.2017.11.263

[32] F. Bobbert, K. Lietaert, A.A. Eftekhari, B. Pouran, S. Ahmadi, H. Weinans, A. Zadpoor, Additively manufactured metallic porous biomaterials based on minimal surfaces: A unique combination of topological, mechanical, and mass transport properties, Acta Biomater., 53 (2017) 572-584. https://doi.org/10.1016/j.actbio.2017.02.024

[33] M. Dias, P. Fernandes, J. Guedes, S. Hollister, Permeability analysis of scaffolds for bone tissue engineering, J. Biomech., 45 (2012) 938-944. https://doi.org/10.1016/j.jbiomech.2012.01.019

[34] S. Ahmadi, S. Yavari, R. Wauthle, B. Pouran, J. Schrooten, H. Weinans, A. Zadpoor, Additively Manufactured Open-Cell Porous Biomaterials Made from Six Different Space-Filling Unit Cells: The Mechanical and Morphological Properties, Materials, 8 (2015) 1871-1896. https://doi.org/10.3390/ma8041871

[35] M. Suard, G. Martin, P. Lhuissier, R. Dendievel, F. Vignat, J.J. Blandin, F. Villeneuve, Mechanical equivalent

diameter of single struts for the stiffness prediction of lattice structures produced by Electron Beam Melting, Addit. Manuf., 8 (2015) 124-131. https://doi.org/10.1016/j.addma.2015.10.002

[36] R.W. Goulet, S.A. Goldstein, M.J. Ciarelli, J.L. Kuhn, M. Brown, L. Feldkamp, The relationship between the structural and orthogonal compressive properties of trabecular bone, J. Biomech., 27 (1994) 379-389. https://doi.org/10.1016/0021-9290(94)90014-0

[37] A.J. Beaudoin, W.M. Mihalko, W.R. Krause, Finite element modelling of polymethylmethacrylate flow through cancellous bone, J. Biomech., 24 (1991) 127-129. https://doi.org/10.1016/0021-9290(91)90357-S

[38] K.-W. Lee, S. Wang, L. Lu, E. Jabbari, B.L. Currier, M.J. Yaszemski, Fabrication and characterization of poly (propylene fumarate) scaffolds with controlled pore structures using 3-dimensional printing and injection molding, Tissue Eng., 12 (2006) 2801-2811. https://doi.org/10.1089/ten.2006.12.2801

[39] C.G. Jeong, H. Zhang, S.J. Hollister, Three-dimensional poly (1, 8-octanediol–co-citrate) scaffold pore shape and permeability effects on sub-cutaneous in vivo chondrogenesis using primary chondrocytes, Acta Biomater., 7 (2011) 505-514. https://doi.org/10.1016/j.actbio.2010.08.027

[40] A.L. Olivares, E. Marsal, J.A. Planell, D. Lacroix, Finite element study of scaffold architecture design and culture conditions for tissue engineering, Biomaterials, 30 (2009) 6142-6149. https://doi.org/10.1016/j.biomaterials.2009.07.041

[41] E.F. Morgan, H.H. Bayraktar, T.M. Keaveny, Trabecular bone modulus–density relationships depend on anatomic site, J. Biomech., 36 (2003) 897-904. https://doi.org/10.1016/S0021-9290(03)00071-X

[42] V. Karageorgiou, D. Kaplan, Porosity of 3D biomaterial scaffolds and osteogenesis, Biomaterials, 26 (2005) 5474-5491. https://doi.org/10.1016/j.biomaterials.2005.02.002

[43] S. Van Bael, Y.C. Chai, S. Truscello, M. Moesen, G. Kerckhofs, H. Van Oosterwyck, J.-P. Kruth, J. Schrooten, The effect of pore geometry on the in vitro biological behavior of human periosteum-derived cells seeded on selective

laser-melted Ti6Al4V bone scaffolds, Acta Biomater., 8 (2012) 2824-2834. https://doi.org/10.1016/j.actbio.2012.04.001

[44] P. Heinl, C. Körner, R.F. Singer, Selective Electron Beam Melting of Cellular Titanium: Mechanical Properties, Adv. Eng. Mater., 10 (2008) 882-888. https://doi.org/10.1002/adem.200800137

[45] G. Campoli, M. Borleffs, S.A. Yavari, R. Wauthle, H. Weinans, A.A. Zadpoor, Mechanical properties of open-cell metallic biomaterials manufactured using additive manufacturing, Mater. & Des., 49 (2013) 957-965. https://doi.org/10.1016/j.matdes.2013.01.071

[46] A.A. Zadpoor, R. Hedayati, Analytical relationships for prediction of the mechanical properties of additively manufactured porous biomaterials, J.Biomed. Mater. Res. A, 104 (2016) 3164-3174. https://doi.org/10.1002/jbm.a.35855

[47] J. Kadkhodapour, H. Montazerian, A. Darabi, A.P. Anaraki, S.M. Ahmadi, A.A. Zadpoor, S. Schmauder, Failure mechanisms of additively manufactured porous biomaterials: Effects of porosity and type of unit cell, J. Mech. Behav. Biomed. Mater., 50 (2015) 180-191. https://doi.org/10.1016/j.jmbbm.2015.06.012

[48] X.-N. Gu, Y.-F. Zheng, A review on magnesium alloys as biodegradable materials, Front. Mater. Sci. China, 4 (2010) 111-115. https://doi.org/10.1007/s11706-010-0024-1

[49] J. Parthasarathy, B. Starly, S. Raman, A. Christensen, Mechanical evaluation of porous titanium (Ti6Al4V) structures with electron beam melting (EBM), J. Mech. Behav. Biomed. Mater., 3 (2010) 249-259. https://doi.org/10.1016/j.jmbbm.2009.10.006

[50] L. Liu, P. Kamm, F. García-Moreno, J. Banhart, D. Pasini, Elastic and failure response of imperfect three-dimensional metallic lattices: the role of geometric defects induced by Selective Laser Melting, J. Mech. Phys. Solids, 107 (2017) 160-184. https://doi.org/10.1016/j.jmps.2017.07.003

[51] V. Weißmann, R. Bader, H. Hansmann, N. Laufer, Influence of the structural orientation on the mechanical

properties of selective laser melted Ti6Al4V open-porous scaffolds, Materials & Design, 95 (2016) 188-197.

https://doi.org/10.1016/j.matdes.2016.01.095

Figures

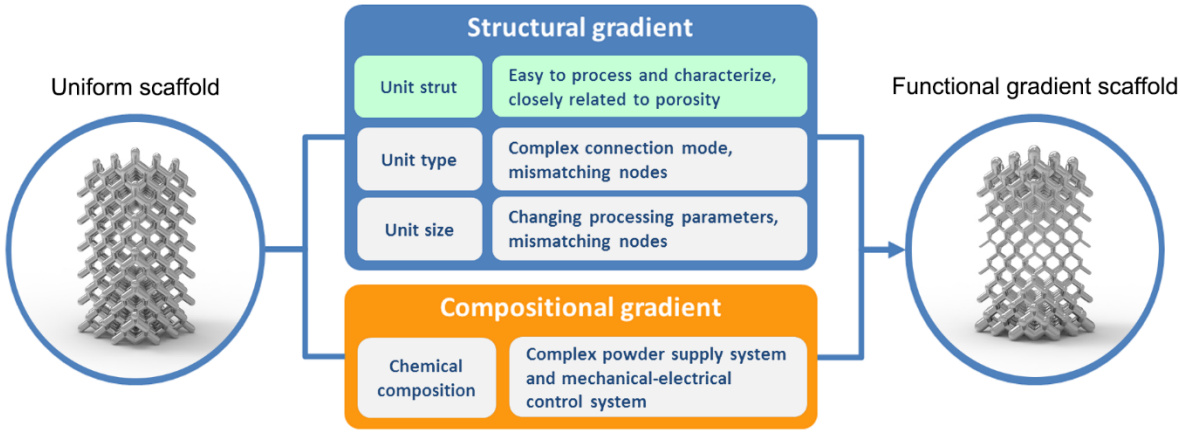

Fig. 1 Schematic diagram of design strategies for FGS and their main pros and cons.

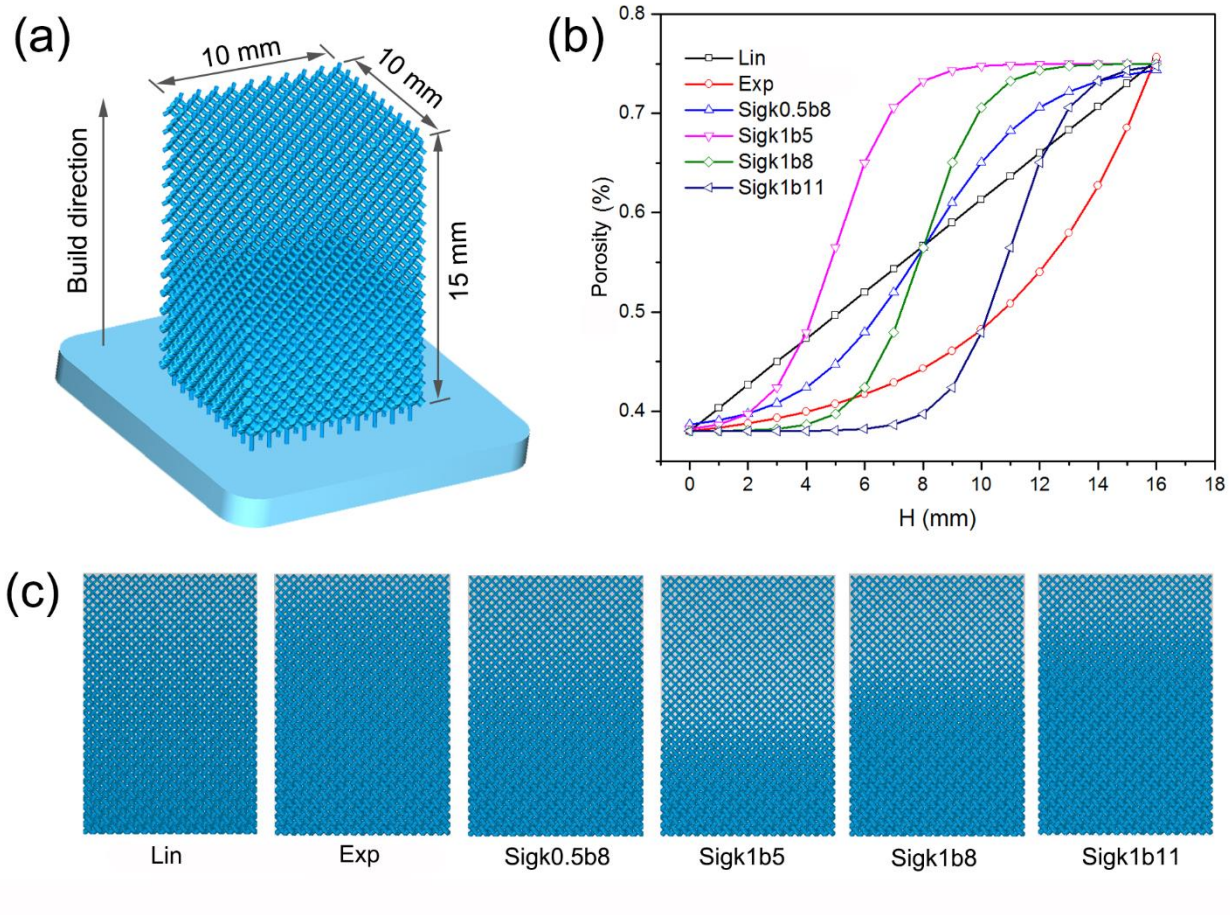

Fig. 2 Designed FGSs: (a) FGS scaffold on the build plate, (b) porosity variations of FGSs in the sample height (H)

direction and (c) front view of FGSs designed with different porosity variation strategies.

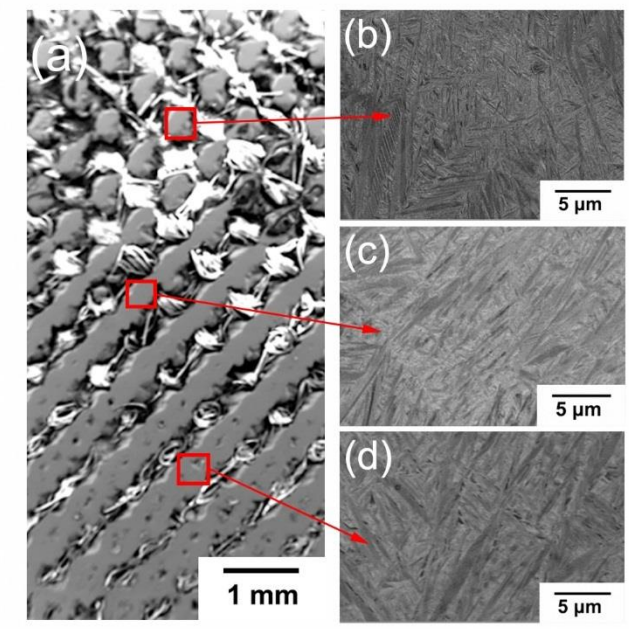

Fig. 3 (a) SEM image of a graded porous structure with a sigmoid function and the microstructures of the areas with porosities of (b) 70%, (c) 55% and (d) 41%.

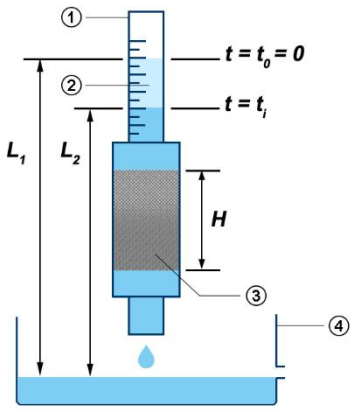

Fig. 4 Schematic representation of the permeability experimental setup using the falling head method.

Permeability values of eighteen samples were measured (three samples for every porosity transition).

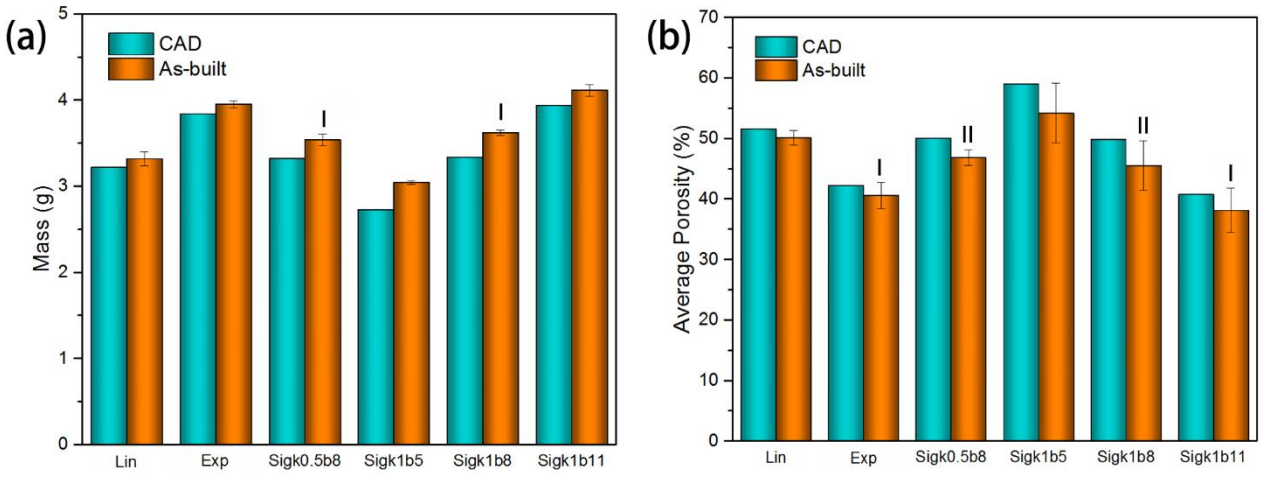

Fig. 5 Comparison between CAD designs and the as-built samples in: (a) mass and (b) average porosity. The test groups marked with the same letter (I or II) are not significantly different ($p>0.05$) (one-way ANOVA, Tukey's test).

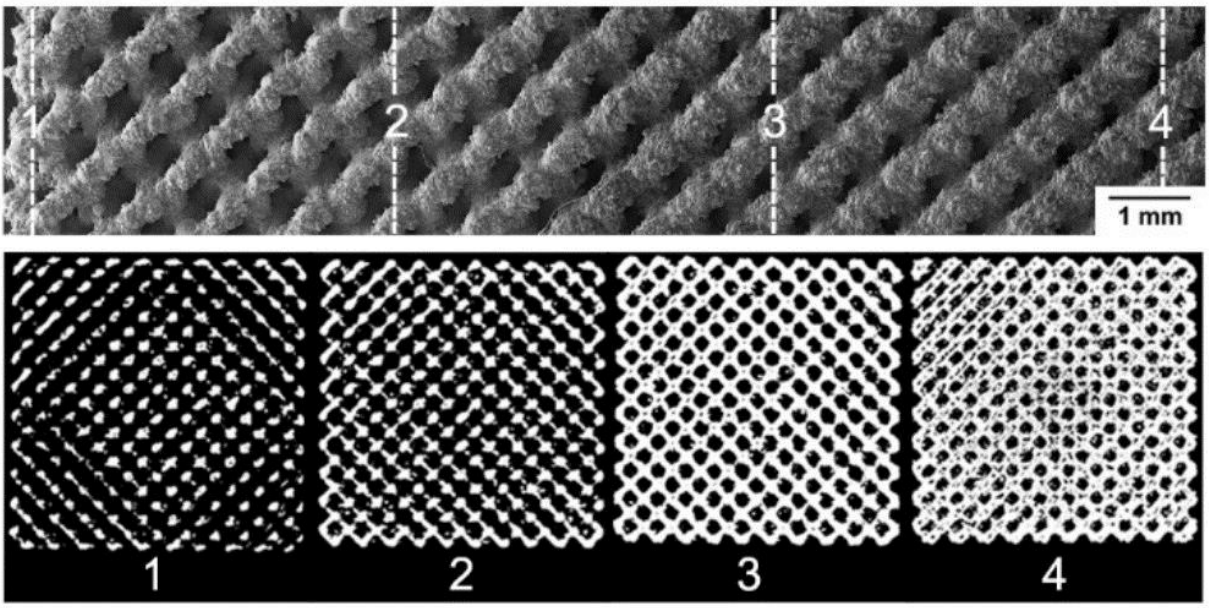

Fig. 6 SEM sideview of sample Sigk0.5b8 (top) and micro-CT 8-bit images of cross-section views (bottom; 1: porosity=74.3%; 2: porosity=65.0%; 3: porosity=44.8%; 4: porosity=39.3%).

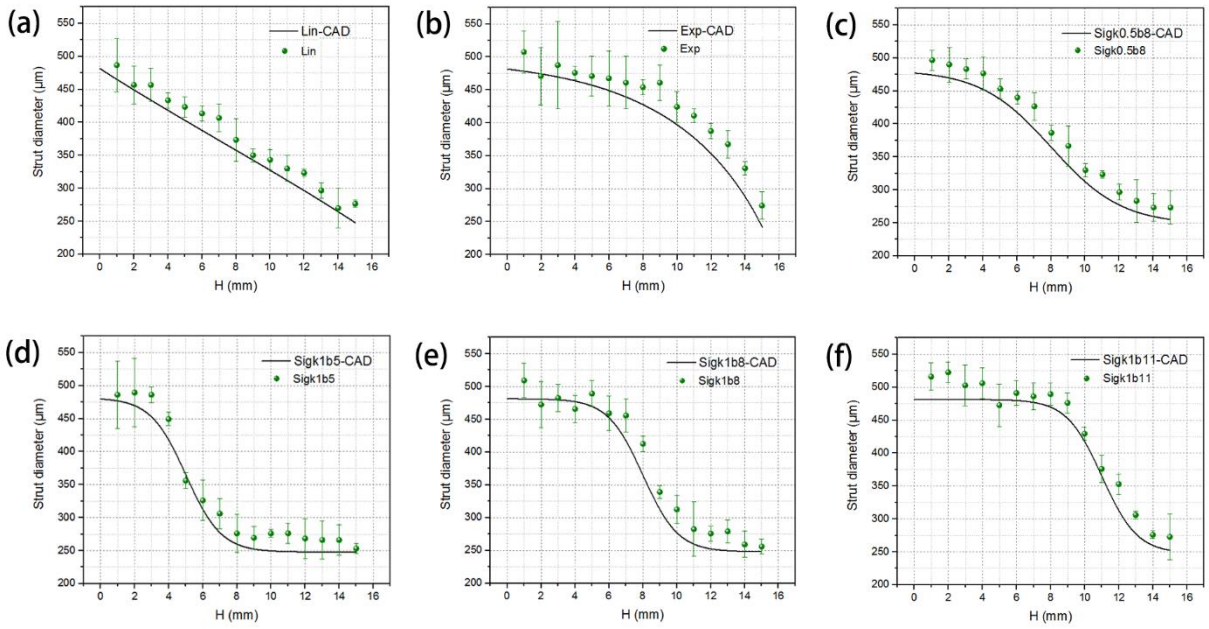

Fig. 7 Comparison in the variation of strut diameter with sample height between CAD design and the as-built samples: (a) Lin, (b) Exp, (c) Sigk0.5b8, (d) Sigk1b5, (e) Sigk1b8 and (f) Sigk1b11.

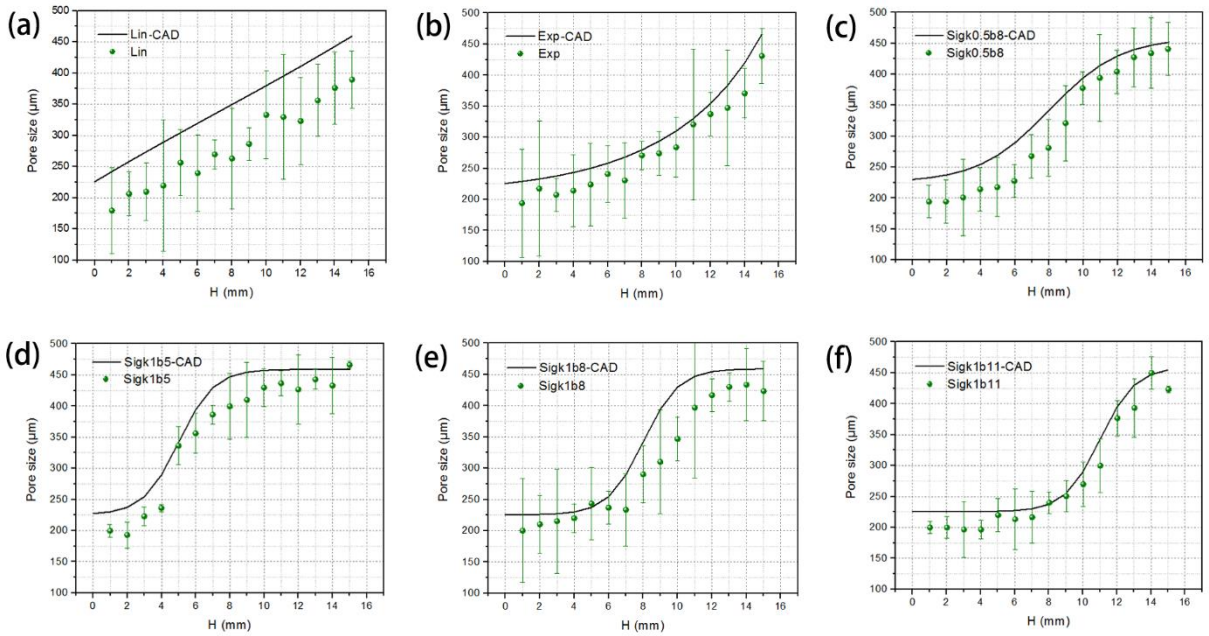

Fig. 8 Comparsion in the varirations of pore size with sample height between CAD design and the as-built samples:

(a) Lin, (b) Exp, (c) Sigk0.5b8, (d) Sigk1b5, (e) Sigk1b8 and (f) Sigk1b11.

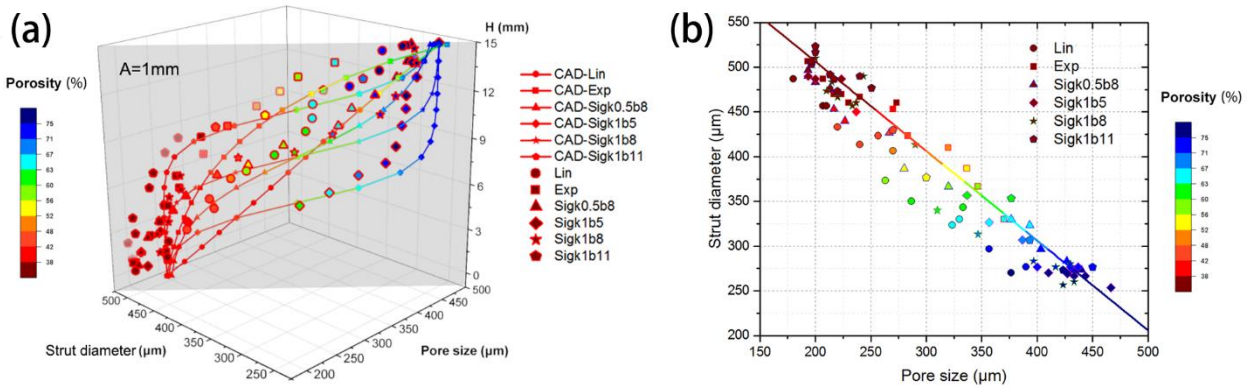

Fig. 9 (a) Variations of strut diameter and pore size with sample height (*H*), in which porosity is expressed by contour legend, and (b) a projection of the data points in (a) on a selected strut diameter-pore size plane.

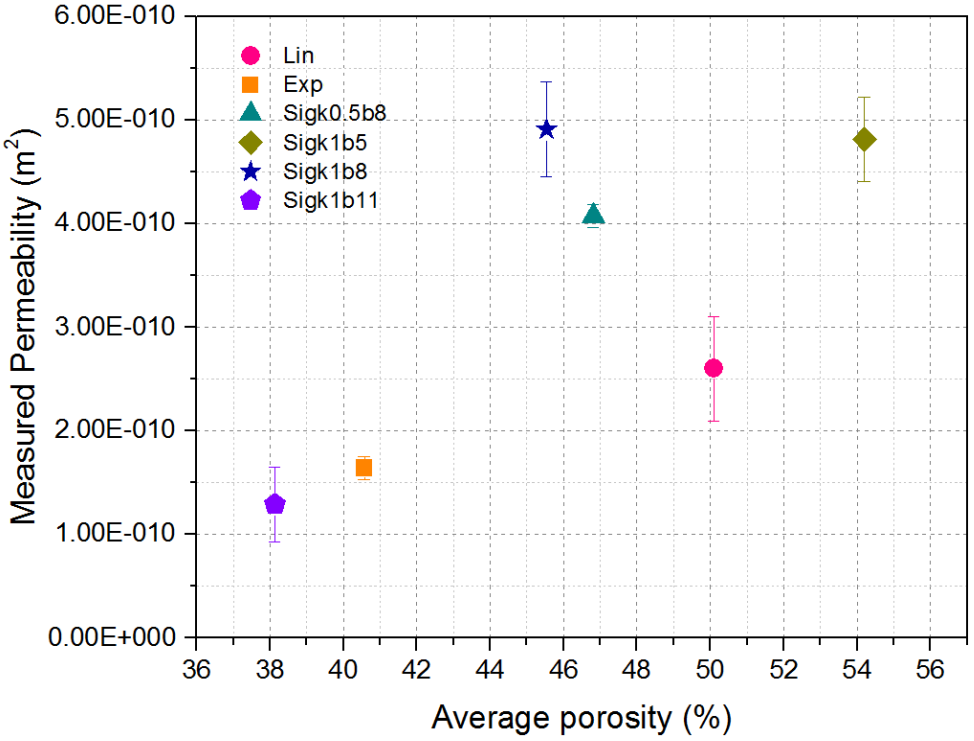

Fig. 10 Permeability of functionally graded scaffolds.

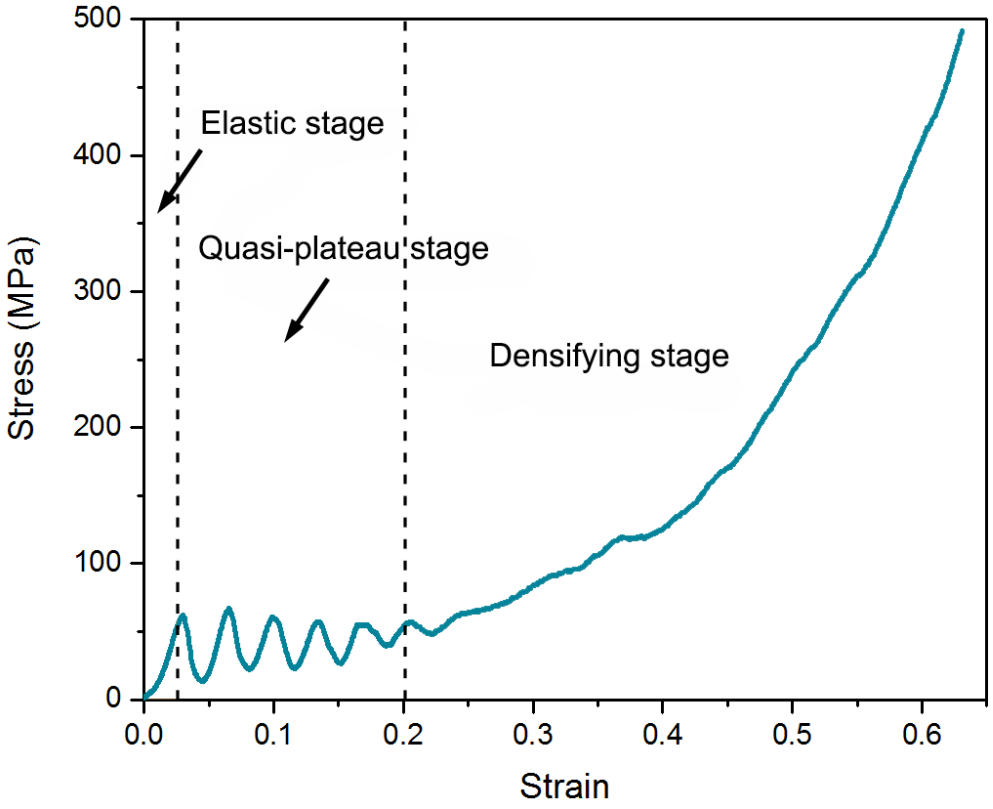

Fig. 11 A schematic compression stress-strain curve of sample Sigk1b5.

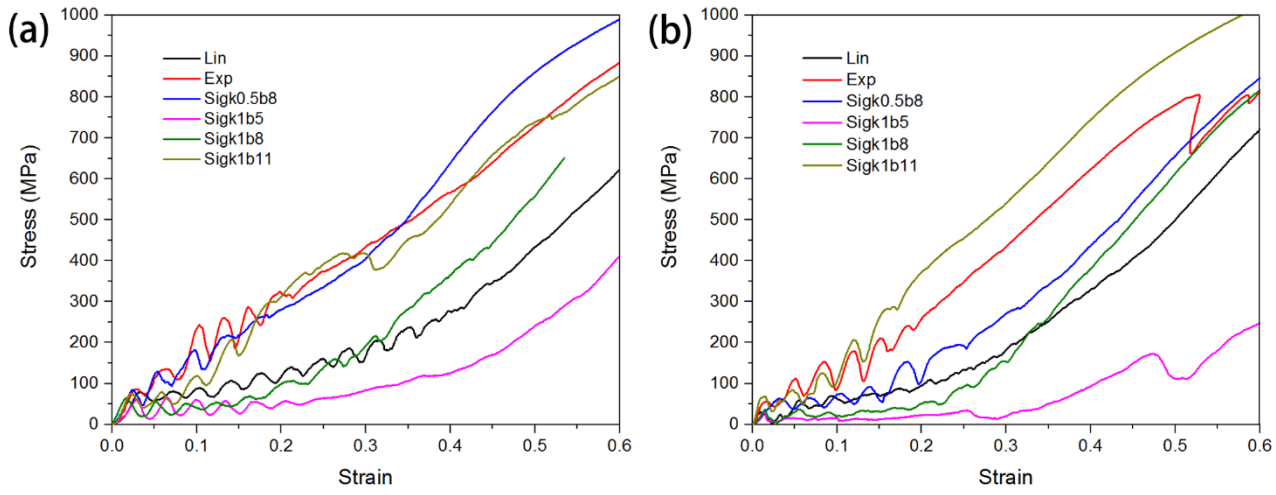

Fig. 12 Stress-strain curves of (a) the as-built and (b) the as-heat-treated samples.

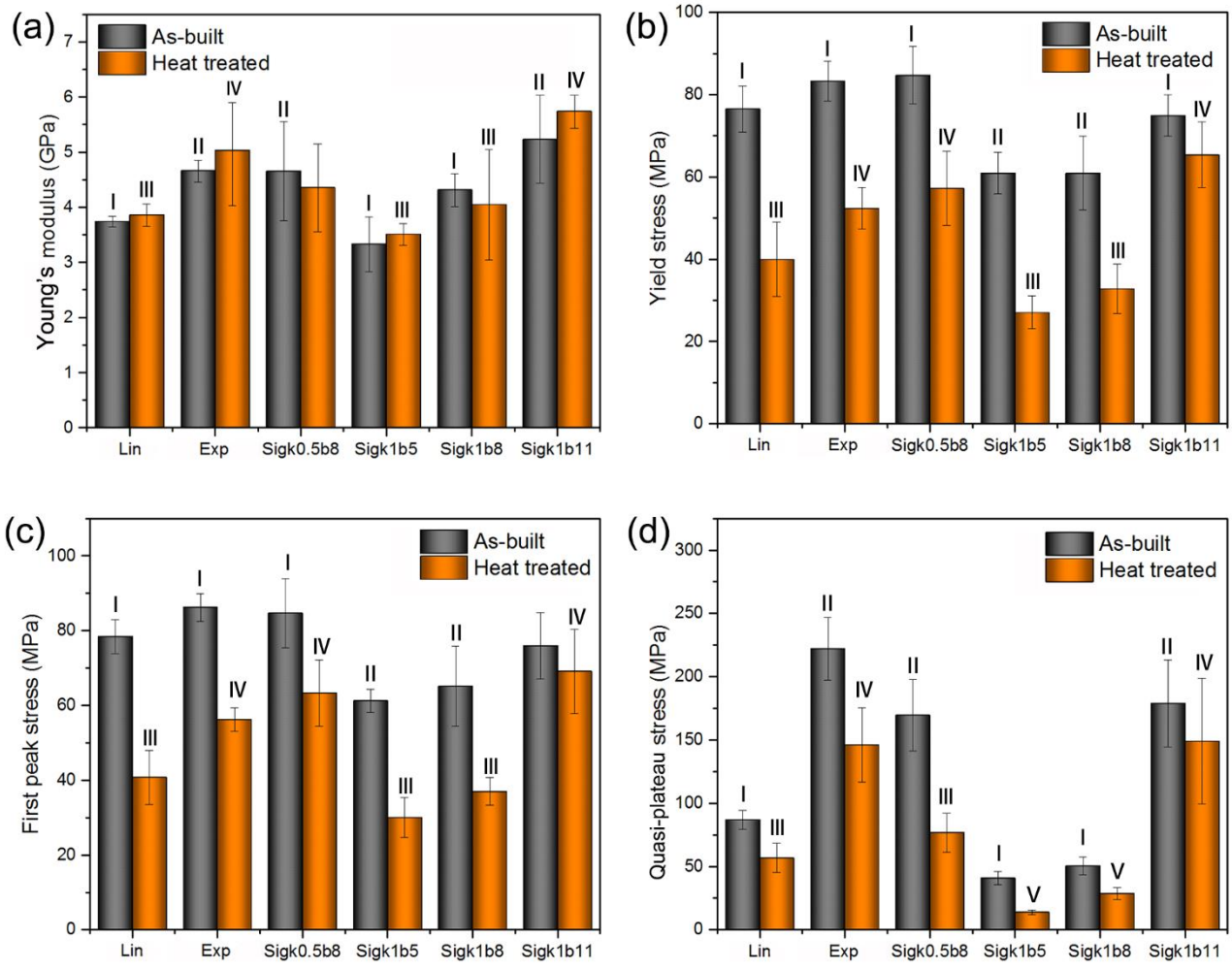

Fig. 13 Mechanical properties of the FGSs: (a) Young's modulus, (b) yield strength, (c) first peak stress and (d) quasi-plateau stress. The test groups marked with the same letter (I, II, III, IV and V) are not significantly different ($p>0.05$) (one-way ANOVA, Tukey's test).

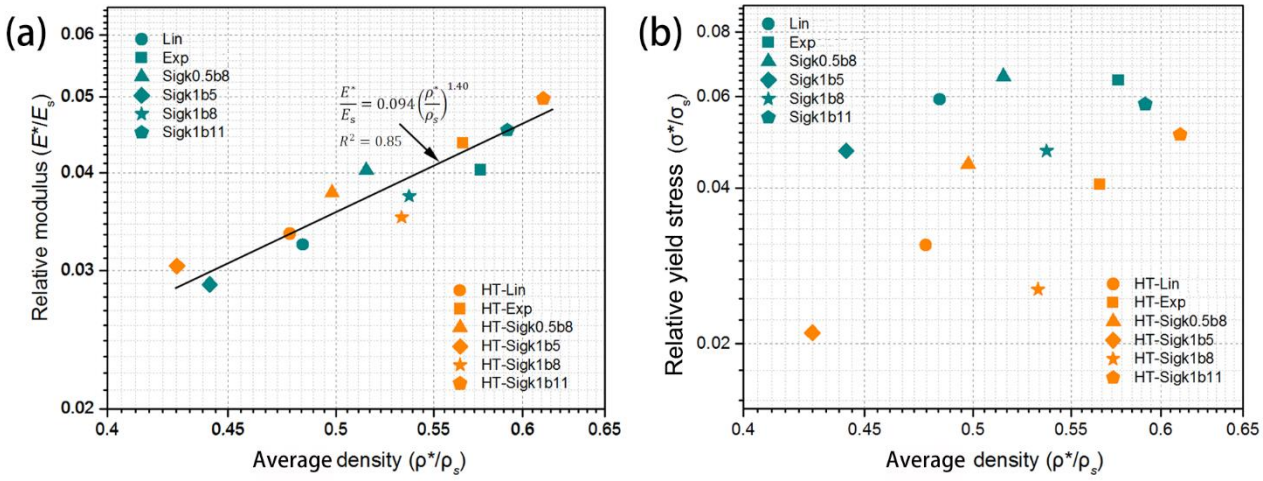

Fig. 14 (a) Relative Young's modulus and (b) relative yield strength in relation to the overall density of the FGSs.

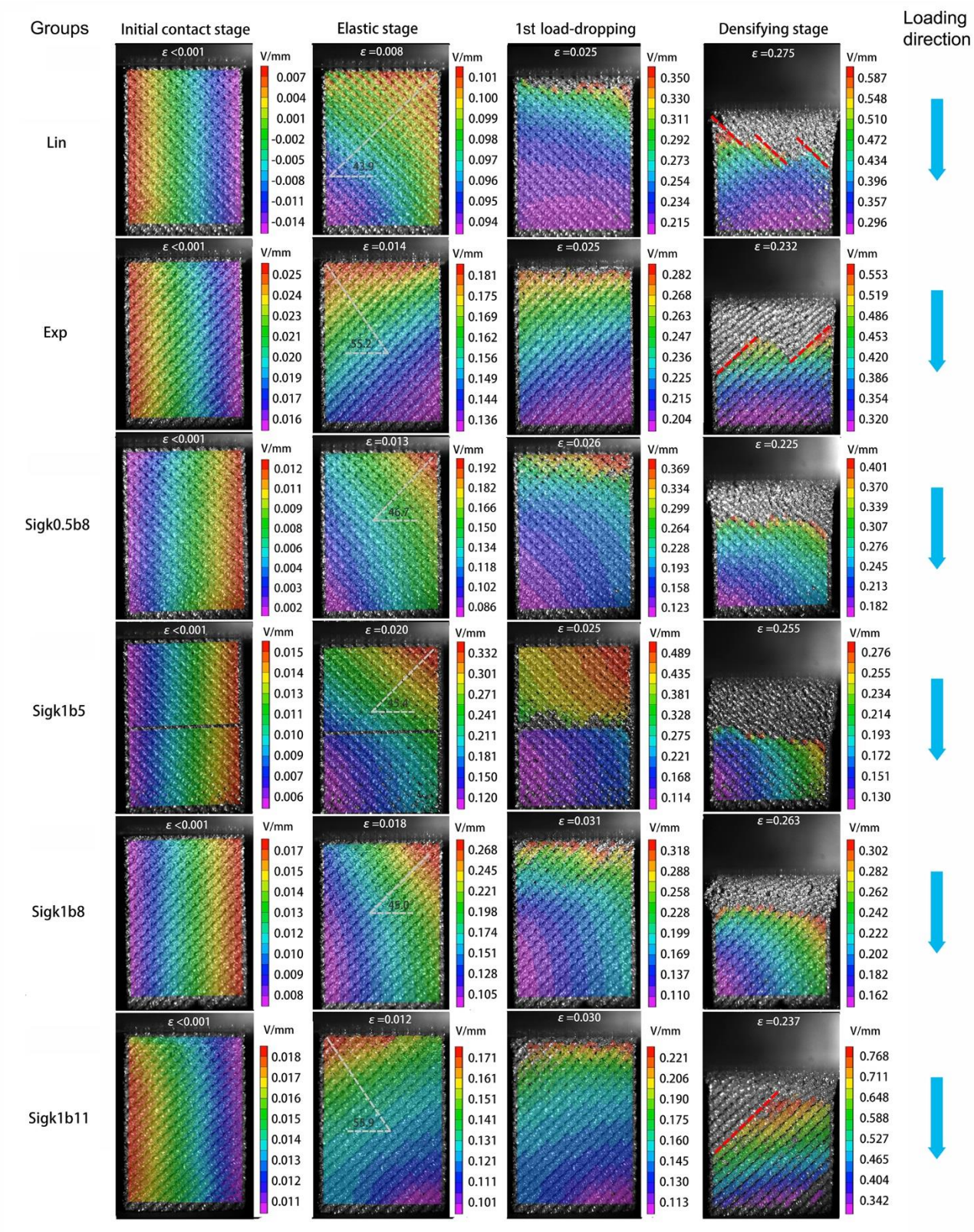

Fig. 15 Vertical displacement (d_v) contour at the four stages of the stress-strain curve of every specimen during compression testing: initial contact stage, elastic stage, 1th load dropping stage and densification stage (from left to

right). The angle between the direction of the vertical displacement gradient and horizontal plane is marked in the elastic stage column with gray lines. The 45° inclined failure planes are marked in the densifying stage column with red lines.

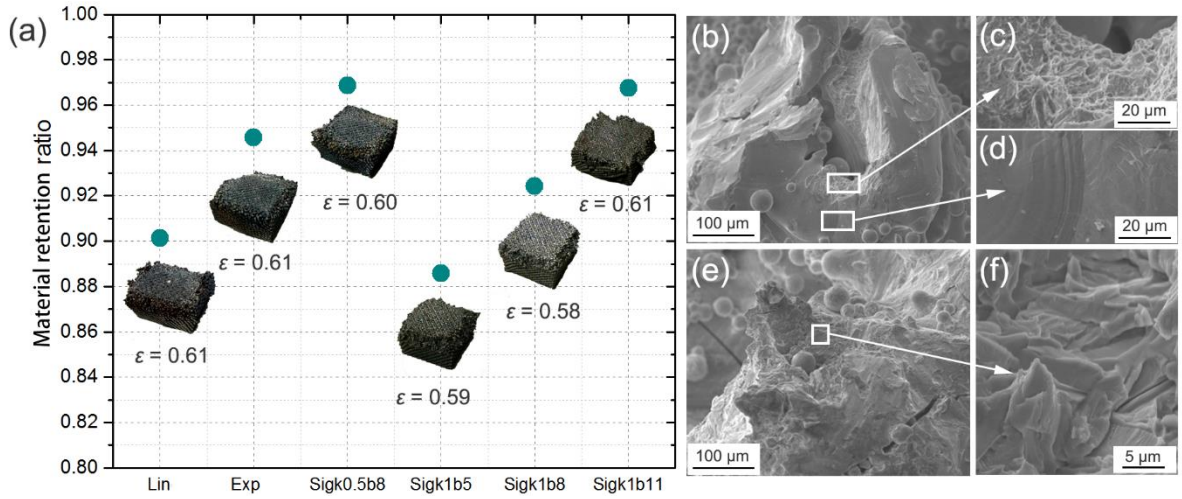

Fig. 16 (a) Material retention ratio of FGS specimens with increasing compressive strain and fracture surfaces of (b) the as-built and (e) as-heat-treated samples Sigk0.5b8 and characteristics of (c) dimple fracture, (d) river-like brittle fracture and (e, f) intergranular fracture.

Table 1. Parameters used in the porosity control equations

Sample groups	Parameters
Lin	A=B=0, C=0.023, D=0.38
Exp	a=0.016, A=B=0, C=0.2, b=0.364
Sigk0.5b8	k=0.5, b=8
Sigk1b5	k=1, b=5
Sigk1b8	k=1, b=8
Sigk1b11	k=1, b=11

Table 2. SLM process parameters

Processing parameters	Values
Laser power	100 W
Spot diameter	50 μm
Layer thickness	50 μm
Hatching space	70 μm
Exposure time	125 μs

Table 3. Parameter values used in permeability experiments

Parameters	Values
Height of sample (H)	15 mm
Cross section of standpipe (a)	4.5×10^{-3} m^2
Cross section of sample (A)	10^{-4} m^2
Dynamic viscosity coefficient of water (μ)	10^{-3} Pa·s
Density of water (ρ)	10^3 kg/m^3
Gravity acceleration (g)	9.8 m/s^2

Table 4 Comparisons between the permeability values of the FGSs and those in other studies

Materials	Porosity (%)	Pore size (μm)	Permeability (m^2)	Ref.
Diamond-FGS	38-75	200-450	$0.129\text{-}0.491\times10^{-9}$	-
Diamond-TPMS	44	413	0.40×10^{-9}	[32]
	48	427	0.58×10^{-9}	
	52	429	0.70×10^{-9}	
	60	370	0.79×10^{-9}	
Cube	30	400	0.078×10^{-9}	[33]
	50	500	0.34×10^{-9}	
	70	700	2.04×10^{-9}	
Human proximal tibia	50-93	-	$0.467\text{-}14.8\times10^{-9}$	[37]

Supplementary information of uniform scaffolds and data summary

Table S1. Morphometric parameters of samples P1 and P2 with uniform lattice structures

	Mass (g)	$\bar{\rho}$ (%) CAD	$\bar{\rho}$ (%) Micro-CT	D_S (μm) CAD	D_S (μm) Micro-CT	D_P (μm) CAD	D_P (μm) Micro-CT
P1	2.69±0.07	63	62.0±1.0	307	384±54	400	390±55
P2	3.44±0.02	53	48.8±0.9	377	423±39	330	306±36

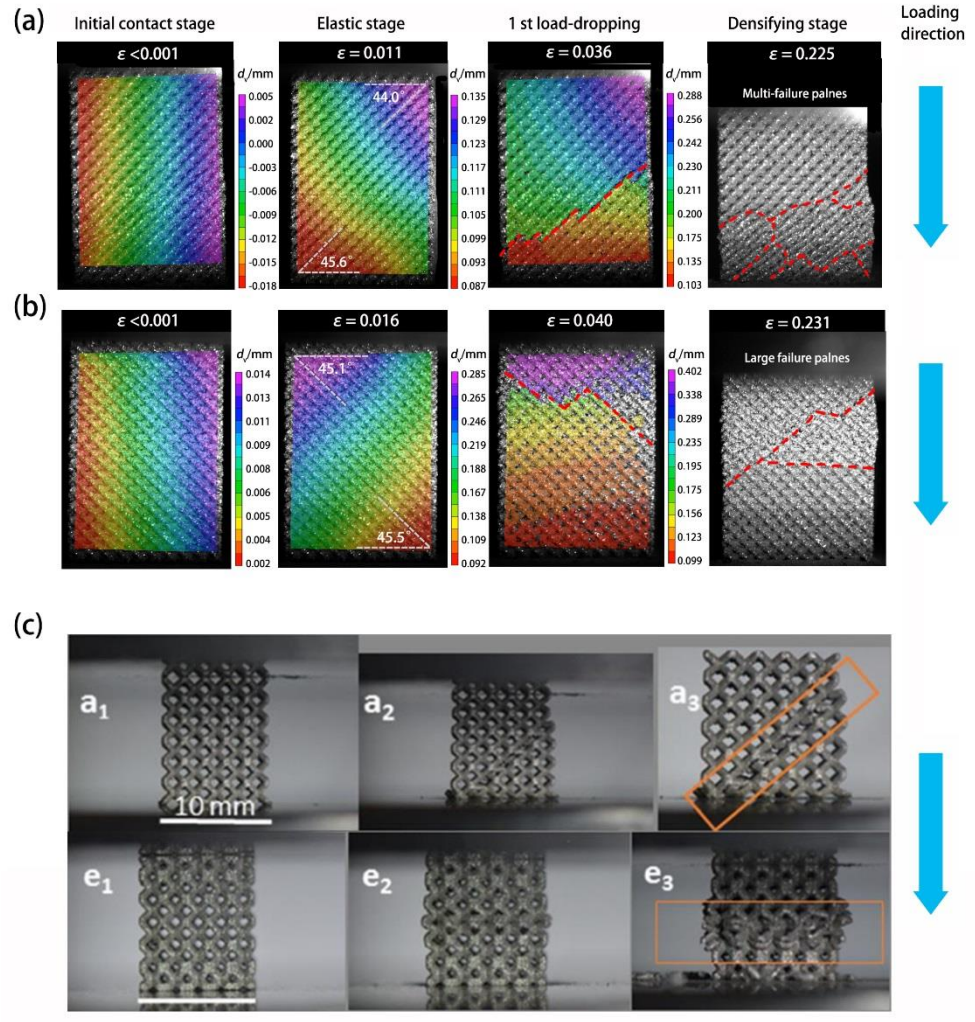

Fig S1. Vertical displacement (d_v) contour of samples P1 (a) and P2 (b) at the four stages of the stress-strain curve of every specimen during compression testing: initial contact stage, elastic stage, 1th load dropping stage and densification stage (from left to right). The angle between the direction of the vertical displacement gradient and horizontal plane is marked in the elastic stage column with gray lines. The 45° inclined failure planes are marked in the densifying stage column with red lines. (c) Failure modes of U0.4 (a_1-a_3) and Dense-Out structure (e_1-e_3) [1]. Left images (subscript 1) represent the initial state and middle (subscript 2) and last right images (subscript 3) present the progressive failure. Highlights represent the observed regions of deformation and failure. (Scale bars = 10 mm).

Table S2 Comparisons in mechanical and physical properties between FGSs, uniform scaffolds and human bone tissue

Specimen	Mass (g)	$\bar{\rho}$ (%)	H_B (mm)	D_S (μm)	D_P (μm)	E (GPa)		σ_s (MPa)		σ_{max} (MPa)		σ_{pl} (MPa)		Permeability (10^{-10} m^2)
						AB	HT	AB	HT	AB	HT	AB	HT	
Lin	3.32±0.08	50.1±1.2	-	276±16 ~ 486±40	180±69 ~ 390±46	3.7±0.1	3.8±0.2	76.6±5.6	40.0±9	78.4±4.5	40.8±7.2	86.9±7.5	56.7±11.7	2.6±0.4
Exp	3.95±0.04	40.6±2.2	-	273±21 ~ 506±32	193±87 ~ 430±45	4.7±0.2	5.0±0.9	83.3±4.8	52.4±5	86.2±3.7	56.2±3.2	222.1±24	145.9±29	1.6±0.1
Sigk0.5b8	3.53±0.07	46.8±1.3	8	273±25 ~ 497±15	193±27 ~ 440±43	4.6±0.9	4.4±0.8	84.7±7.1	57.3±9	84.7±9.3	63.3±8.9	169.5±28	76.9±15	4.1±0.1
Sigk1b5	3.04±0.02	54.2±4.9	5	254±8 ~ 486±51	200±10 ~ 466±16	3.3±0.5	3.5±0.2	60.9±5.3	27.1±4	61.3±3.1	30.1±5.3	40.9±5.4	14.0±1.8	4.8±0.4
Sigk1b8	3.62±0.03	45.5±4.1	8	256±12 ~ 510±26	200±83 ~ 423±48	4.3±0.3	4.0±0.8	64.9±9.0	32.8±6	65.2±10.7	37.0±3.7	50.5±7.2	28.6±4.8	4.9±0.4
Sigk1b11	4.11±0.07	38.1±3.7	11	273±35 ~ 516±21	200±10 ~ 423±16	5.2±0.8	5.7±0.3	74.9±5.5	65.4±8	76.0±8.9	69.1±11.2	178.9±34	149.1±50	1.3±0.3
P1	2.69±0.07	62.0±1.0	-	384±54	390±55	3.8±0.1	-	75±3.8	-	111.5±10.5	-	70.0±5.2	-	4.1±0.01
P2	3.44±0.02	48.8±0.9	-	423±39	306±36	6.5±0.6	-	155±15.3	-	179.2±9.9	-	125.9±35.3	-	2.6±0.02
Trabecular bone	-	-	-	100-190 [2]	320 ~ 1670 [2]	0.01 ~ 1.57 [3]		55.3±8.6 [4]		-	-			4.67-148 [5]
Cortical bone	-	-	-	-	-	5-23 [3]		164-240 [3]		-	-			-

*$\bar{\rho}$: average porosity, H_B: height of the transition boundary, D_S: strut diameter, D_P: pore size, AB: as-built samples, HT: heat treated samples

Reference:

[1] E. Onal, J.E. Frith, M. Jurg, X. Wu, A. Molotnikov, Mechanical Properties and In Vitro Behavior of Additively Manufactured and Functionally Graded Ti6Al4V Porous Scaffolds, Metals, 8 (2018) 200.

[2] R.W. Goulet, S.A. Goldstein, M.J. Ciarelli, J.L. Kuhn, M. Brown, L. Feldkamp, The relationship between the structural and orthogonal compressive properties of trabecular bone, J. Biomech., 27 (1994) 379-389.

[3] X.-N. Gu, Y.-F. Zheng, A review on magnesium alloys as biodegradable materials, Frontiers of Materials Science in China, 4 (2010) 111-115.

[4] E.F. Morgan, H.H. Bayraktar, T.M. Keaveny, Trabecular bone modulus–density relationships depend on anatomic site, J. Biomech., 36 (2003) 897-904.

[5] A.J. Beaudoin, W.M. Mihalko, W.R. Krause, Finite element modelling of polymethylmethacrylate flow through cancellous bone, J. Biomech., 24 (1991) 127-129.